1 **Do surface lateral flows matter for data assimilation of soil moisture observations**

2 **into hyperresolution land models?**

3 **Running title: HYPERRESOLUTION LAND DATA ASSIMILATION**

4 Yohei Sawada[1,2],

5 [1] Institute of Engineering Innovation, the University of Tokyo, Tokyo, Japan

6 [2] Meteorological Research Institute, Japan Meteorological Agency, Tsukuba, Japan

9 Corresponding author: Y. Sawada, Institute of Engineering Innovation, the University of

10 Tokyo, Tokyo, Japan, 2-11-6, Yayoi, Bunkyo-ku, Tokyo, Japan, yohei.sawada@sogo.t.u-

11 tokyo.ac.jp

13   **Abstract**

14   It is expected that hyperresolution land modeling substantially innovates the simulation

15   of terrestrial water, energy, and carbon cycles. The major advantage of hyperresolution

16   land models against conventional one-dimensional land surface models is that

17   hyperresolution land models can explicitly simulate lateral water flows. Despite many

18   efforts on data assimilation of hydrological observations into those hyperresolution land

19   models, how surface water flows driven by local topography matter for data assimilation

20   of soil moisture observations has not been fully clarified. Here I perform two minimalist

21   synthetic experiments where soil moisture observations are assimilated into an integrated

22   surface-groundwater land model by an ensemble Kalman filter. I discuss how differently

23   the ensemble Kalman filter works when surface lateral flows are switched on and off. A

24   horizontal background error covariance provided by overland flows is important to adjust

25   the unobserved state variables (pressure head and soil moisture) and parameters (saturated

26   hydraulic conductivity). However, the non-Gaussianity of the background error provided

27   by the nonlinearity of a topography-driven surface flow harms the performance of data

28   assimilation. It is difficult to efficiently constrain model states at the edge of the area

29   where the topography-driven surface flow reaches by linear-Gaussian filters. It brings the

30   new challenge in land data assimilation for hyperresolution land models. This study

31   highlights the importance of surface lateral flows in hydrological data assimilation.

34   **1. Introduction**

35   Hyperresolution land modeling is expected to improve the simulation of terrestrial water,

36   energy, and carbon cycles, which is crucially important for meteorological, hydrological

37   and ecological applications (see Wood et al. (2011) for a comprehensive review). While

38   conventional land surface models (LSMs) assume that lateral water flows are negligible

39   at the coarse resolution (>25km) and solve vertical one-dimensional Richards equation

40   for the soil moisture simulation (e.g., Sellers et al. 1996; Lawrence et al. 2011), currently

41   proposed hyperresolution land models, which can be applied at a finer resolution (<1km),

42   explicitly consider surface and subsurface lateral water flows (e.g., Maxwell and Miller

43   2005; Tian et al. 2012; Shrestha et al. 2014; Niu et al. 2014). The fine horizontal resolution

44   can resolve slopes, which are drivers of a lateral transport of water, and realize the fully

45   integrated surface-groundwater modeling. Previous works indicated that a lateral

46   transport of water strongly controls latent heat flux and the partitioning of

47   evapotranspiration into base soil evaporation and plant transpiration (e.g., Maxwell and

48   Condon 2016; Ji et al. 2017; Fang et al. 2017). This effect of a lateral transport of water

49   on land-atmosphere interactions has been recognized (e.g., Williams and Maxwell 2011;

50   Keune et al. 2016).

52   Data assimilation has contributed to improving the performance of LSMs by fusing

53   simulation and observation. The grand challenge of land data assimilation is to improve

54   the simulation of unobservable variables using observations by propagating observations'

55   information into model's high dimensional state and parameter space. In previous works

56   on the conventional 1-D LSMs, many land data assimilation systems (LDASs) have been

57   proposed to accurately estimate model's state and parameter variables, which cannot be

58   directly observed, by assimilating satellite and in-situ observations. For example, the

59   optimization of LSM's unknown parameters (e.g., hydraulic conductivity) has been

60   implemented by assimilating remotely sensed microwave observations (e.g., Yang et al.

61   2007; Yang et al. 2009; Bandara et al. 2014; Bandara et al. 2015; Sawada and Koike 2014;

62   Han et al. 2014). Kumar et al. (2009) focused on the correlation between surface and root-

63   zone soil moistures to examine the potential of assimilating surface soil moisture

64   observations to estimate root-zone soil moisture. Sawada et al. (2015) successfully

65   improved the simulation of root-zone soil moisture by assimilating microwave brightness

66   temperature observations which include the information of vegetation water content.

67   Gravity Recovery and Climate Experiment total water storage observation has been

68   intensively used to improve the simulation of groundwater and soil moisture (e.g., Li et

69   al. 2012; Houborg et al. 2012). Improving the simulation of state variables such as soil

70   moisture and biomass by LDASs has contributed to accurately estimating fluxes such as

71   evapotranspiration (e.g. Martens et al. 2017) and CO_2 flux (e.g., Verbeeck et al. 2011).

72   However, in most of the studies on the conventional 1-D LDASs, observations impacted

73   state variables and parameters only in a single model's horizontal grid which is identical

74   to the location of the observation. The assumption that the water flows are restricted to

75   vertical direction in LSMs makes it difficult to propagate observation's information

76   horizontally. It limits the potential of land data assimilation to fully use land hydrological

77   observations.

78

79   The hyperresolution land models, which explicitly solve surface and subsurface lateral

80   flows, provide a unique opportunity to examine the potential of land data assimilation to

81   propagate observation's information horizontally in a model space and efficiently use land

82   hydrological observations. Previous works successfully applied Ensemble Kalman Filters

83   (EnKF) to 3-D Richards' equation-based integrated surface-groundwater models. For

84   example, Camporese et al. (2009) and Camporese et al. (2010) successfully assimilated

85   synthetic observations of surface pressure head and streamflow into the Catchment

86   Hydrology (CATHY). Ridler et al. (2014) successfully assimilated Soil Moisture and

87   Ocean Salinity satellite-observed surface soil moisture into the MIKE SHE distributed

88   hydrological model (see also Zhang et al. (2015)). Kurtz et al. (2016) coupled the Parallel

89   Data Assimilation Framework (PDAF) (Nerger and Hiller 2013) with the Terrestrial

90   System Modelling Framework (TerrSysMP) (Shrestha et al. 2014) and successfully

91   estimate the spatial distribution of soil moisture and saturated hydraulic conductivity in

92   the synthetic experiment (see also Zhang et al. (2018)). In addition, Kurtz et al. (2016)

93   indicated that their EnKF approach is computationally efficient in high-performance

94   computers. Those studies have significantly contributed to fully assimilating the new

95   high-resolution soil moisture observations such as Sentinel-1 (e.g., Paroscia et al. 2013)

96

97   Although the data assimilation of hydrological observations into hyperresolution land

98   models has been successfully implemented in the synthetic experiments, it is unclear how

99   topography-driven surface lateral water flows matter for data assimilation of soil moisture

100   observations. Previous studies on data assimilation with high resolution models mainly

101   focused on assimilating groundwater observations (e.g., Ait-El-Fquih et al. 2016;

102 Rasmussen et al. 2015; Hendricks-Franssen et al. 2008). There are some applications

103 which focused on the observation of soil moisture and pressure head in shallow

104 unsaturated soil layers. However, in those studies, topography-driven surface flow has

105 not been considered in the experiment (Kurtz et al. 2016) or the role of them in

106 assimilating observations into the hyperresolution land models has not been quantitatively

107 discussed (Camporese et al. 2010; Camporese et al. 2009). This study aims at clarifying

108 if surface lateral flows matter for data assimilation of soil moisture observations into

109 hyperresolution land models by a minimalist numerical experiment.

110

111

112 **2. Methods**

113 2.1. Model

114 ParFlow is an open source platform which realizes fully integrated surface-groundwater

115 flow modeling (Kollet and Maxwell 2006; Maxwell et al. 2015). This model can be

116 efficiently parallelized in high performance computers and has been widely used as a core

117 hydrological module in hyperresolution land models (e.g., Maxwell and Kollet 2008;

118 Maxwell and Condon 2016; Fang et al. 2017; Kurtz et al. 2016; Maxwell et al. 2011;

119 Williams and Maxwell 2011; Shrestha et al. 2014). Since I used this widely adopted solver

120   as is and added nothing new to the model physics, I described the method of ParFlow to

121   simulate integrated surface-subsurface water flows briefly and omitted the details of

122   numerical methods. The complete description of ParFlow can be found in Kollet and

123   Maxwell (2006), Maxwell et al. (2015) and references therein.

124

125   In the subsurface, ParFlow solves the variably saturated Richards equation in three

126   dimensions.

127     $S_S S_W(h) \frac{\partial h}{\partial t} + \phi S_W(h) \frac{\partial S_W(h)}{\partial t} = \nabla \cdot \mathbf{q} + q_r$ (1)

128     $\mathbf{q} = -\boldsymbol{K_s}(\boldsymbol{x}) k_r(h) [\nabla(h + z) cos\theta_x + sin\theta_x]$ (2)

129   In equation (1), *h* is the pressure head [L]; z is the elevation with the z axis specified as

130   upward [L]; S_S is the specific storage [L^{-1}]; S_W is the relative saturation; ϕ is the

131   porosity [-]; q_r is a source/sink term. Equation (2) describes the flux $\mathbf{q}$

132   [LT^{-1}] by Darcy's law, and $\boldsymbol{K_s}$ is the saturated hydraulic conductivity tensor [LT^{-1}]; k_r

133   is the relative permeability [-]; θ is the local angle of topographic slope (see Maxwell et

134   al. 2015). In this paper, the saturated hydraulic conductivity is assumed to be isotropic

135   and a function of z:

136     $\boldsymbol{K_s} = K_s(z) = K_{s,surface} \exp\left(-f\left(z_{surface} - z\right)\right)$ (3)

137   where $K_{s,surface}$ is the saturated hydraulic conductivity at the surface soil, and $z_{surface}$

138   is the elevation of the soil surface. The saturated hydraulic conductivity decreases

139   exponentially as the soil depth increases (Beven 1982). A van Genuchten relationship

140   (van Genuchten 1980) is used for the relative saturation and permeability functions.

141    $$S_W(h) = \frac{S_{sat} - S_{res}}{(1+(\alpha h)^n)^{(1-\frac{1}{n})}} + S_{res} \qquad (4)$$

142    $$k_r(h) = \frac{(1 - \frac{(\alpha h)^{n-1}}{(1+(\alpha h)^n)^{(1-\frac{1}{n})}})^2}{(1+(\alpha h)^n)^{\frac{(1-\frac{1}{n})}{2}}} \qquad (5)$$

143   where α [L-1] and n [-] are soil parameters, S_{sat} is the relative saturated water content

144   and S_{res} is the relative residual saturation.

145

146   Overland flow is solved by the two-dimensional kinematic wave equation. The dynamics

147   of the surface ponding depth, h [L], can be described by:

148    $$\mathbf{k} \cdot [-K_s(z)k_r(h) \cdot \nabla(h+z)] = \frac{\partial \|h,0\|}{\partial t} - \nabla \cdot \|h,0\| \boldsymbol{v_{sw}} + q_r \qquad (6)$$

149   In equation (6), $\mathbf{k}$ is the unit vector in the vertical and $\|h,0\|$ indicates the greater value

150   of the two quantities following the notation of Maxwell et al. (2015). This formulation

151   results in the overland flow equation being represented as a boundary condition to the

152   variably saturated Richards equation (Kollet and Maxwell 2006). If h < 0, equation (6)

153   describes that vertical fluxes across the land surface is equal to the source/sink term q_r

154   (i.e., rainfall and evapotranspiration). If h > 0, the terms on the right-hand side of equation

155   (6), which indicate water fluxes routed according to surface topography, are active. v_{sw}

156   is the two-dimensional depth-averaged water flow velocity [LT^{-1}] and estimated by the

157   Manning's law:

158   $$v_{sw,x} = \left(\frac{\sqrt{S_{f,x}}}{n_M} h^{\frac{2}{3}}\right), v_{sw,y} = \left(\frac{\sqrt{S_{f,y}}}{n_M} h^{\frac{2}{3}}\right) \quad (7)$$

159   where $S_{f,x}$ and $S_{f,y}$ are the friction slopes [-] for the x- and y-direction, respectively;

160   n_M is the Manning's coefficient [TL$^{-1/3}$]. In the kinematic wave approximation, the

161   friction slopes are set to the bed slopes. The methodology of discretization and the

162   numerical method to solve equations (1-7) can be found in Kollet and Maxwell (2006).

163

164

165   **2.2. Data Assimilation**

166   In this paper, the ensemble Kalman filter (EnKF) was applied to assimilate soil moisture

167   observations into ParFlow. The EnKF has widely been applied to hyper-resolution land

168   models (e.g., Camporese et al. (2009); Camporese et al. (2010); Ridler et al. (2014);

169   Zhang et al. (2015); Kurtz et al. (2016); Zhang et al. (2018)). I examined if surface lateral

170   flows matter for data assimilation of soil moisture observations into hyperresolution land

171   models using this widely adopted data assimilation method.

172

173   The Parflow model can be formulated as a discrete state-space dynamic system:

174    $$\boldsymbol{x}(t+1) = f\big(\boldsymbol{x}(t), \boldsymbol{\theta}, \boldsymbol{u}(t)\big) + \boldsymbol{q}(t) \qquad (8)$$

175   where $\boldsymbol{x}(t)$ is the state variables (i.e. pressure head), $\boldsymbol{\theta}$ is the time-invariant model

176   parameters (i.e. saturated hydraulic conductivity), $\boldsymbol{u}(t)$ is the external forcing (i.e.,

177   rainfall and evapotranspiration), and $\boldsymbol{q}(t)$ is the noise process which represents the

178   model error. In data assimilation, it is useful to formulate an observation process as

179   follows:

180    $$\boldsymbol{y}^f(t) = \mathcal{H}\big(\boldsymbol{x}(t)\big) + \boldsymbol{r}(t) \qquad (9)$$

181   where $\boldsymbol{y}^f(t)$ is the simulated observation, $\mathcal{H}$ is the observation operator which maps

182   the model's state variables into the observable variables, and $\boldsymbol{r}(t)$ is the noise process

183   which represents the observation error. The purpose of EnKF (and any other data

184   assimilation methods) is to find the optimal state variables $\boldsymbol{x}(t)$ based on the simulation

185    $\boldsymbol{y}^f(t)$ and observation (defined as $\boldsymbol{y}^o$) considering their errors ($\boldsymbol{q}(t)$ and $\boldsymbol{r}(t)$)

186

187   The general description of the Kalman filter is the following:

188    $$\boldsymbol{x}^f(t) = \mathcal{M}[\boldsymbol{x}^a(t-1)] \qquad (10)$$

189    $$\boldsymbol{x}^a(t) = \boldsymbol{x}^f(t) + \boldsymbol{K}[\boldsymbol{y}^o - \mathcal{H}(\boldsymbol{x}^f(t))] \qquad (11)$$

190    $$\boldsymbol{K} = \boldsymbol{P}^f \mathcal{H}^T (\mathcal{H} \boldsymbol{P}^f \mathcal{H}^T + \boldsymbol{R})^{-1} \qquad (12)$$

191     $\boldsymbol{P^a} = (\boldsymbol{I} - \boldsymbol{K\mathcal{H}})\boldsymbol{P^f}$ (13)

192   I follow the notation of Houtekamer and Zhang (2016). Superscripts f and a are forecast

193   and analysis, respectively. In equation (10), a forecast model $\mathcal{M}$ (ParFlow in this study)

194   is used to obtain a prior estimate at time t, $\boldsymbol{x}^f(t)$, from the estimation at the previous time

195     $\boldsymbol{x}^a(t-1)$. In equation (11), a prior estimate $\boldsymbol{x}^f(t)$ is updated to the analysis state,

196     $\boldsymbol{x}^a(t)$, using new observations y^o. The Kalman gain matrix **K,** calculated by equation

197   (12), gives an appropriate weight for the observations with an error covariance matrix $\boldsymbol{R}$,

198   and the prior with an error covariance matrix $\boldsymbol{P^f}$. $\boldsymbol{P^a}$ is an updated analysis error

199   covariance. To calculate **K**, the observation operator $\mathcal{H}$ is needed to map from model

200   space to observation space. It should be noted that the equations (10-13) give an optimal

201   estimation only when the model and observation errors follow the Gaussian distribution.

202   When the probabilistic distribution of the error in either model or observation has a non-

203   Gaussian structure, results of the Kalman filter are suboptimal. This point is important to

204   interpret the results of this study.

205

206   EnKF is the Monte Carlo implementation of equations (10-13). To compute the Kalman

207   gain matrix, **K,** ensemble approximations of $\boldsymbol{P^f\mathcal{H}^T}$ and $\boldsymbol{\mathcal{H}P^f\mathcal{H}^T}$ can be given by:

208     $\boldsymbol{P^f\mathcal{H}^T} \equiv \frac{1}{k-1}\sum_{i=1}^{k}\left(\boldsymbol{x}_i^f - \overline{\boldsymbol{x}^f}\right)\left(\mathcal{H}\boldsymbol{x}_i^f - \overline{\mathcal{H}\boldsymbol{x}^f}\right)^T$ (14)

209    $\mathcal{H}P^f\mathcal{H}^T \equiv \frac{1}{k-1}\sum_{i=1}^{k}\left(\mathcal{H}x_i^f - \overline{\mathcal{H}x^f}\right)\left(\mathcal{H}x_i^f - \overline{\mathcal{H}x^f}\right)^T$ (15)

210   where x_i^f is the ith member of a k-member ensemble prior and $\overline{x^f} = \frac{1}{k}\sum_{i=1}^{k}x_i^f$ and

211    $\overline{\mathcal{H}x^f} = \frac{1}{k}\sum_{i=1}^{k}\mathcal{H}x_i^f$.

212

213   Once $\overline{x^a} = \sum_{i=1}^{k}x_i^a$ (x_i^a is the ith member of a k-member ensemble analysis) and $P^a =$

214    $\frac{1}{k-1}\sum_{i=1}^{k}(x_i^a - \overline{x^a})(x_i^a - \overline{x^a})^T$ are computed by equations (10-15), there are many

215   choices of an analysis ensemble. Although equations (10-15) can calculate the mean and

216   variance of the ensemble members, they do not tell how to adjust the state of the ensemble

217   members in order to realize the estimated mean and variance. There are many proposed

218   flavors of EnKF and one of the differences among them is the method to choose the

219   analysis x_i^a. In this paper, the Ensemble Transform Kalman Filter (ETKF; Bishop et al.

220   2001; Hunt et al. 2007) was used to transport forecast ensembles to analysis ensembles.

221   ETKF has been used for hyperresolution land data assimilation (e.g., Kurtz et al. 2016).

222   Please refer to Hunt et al. (2007) for the complete description of the ETKF and its

223   localized version, the Local Ensemble Transform Kalman Filter (LETKF). The open

224   source available at https://github.com/takemasa-miyoshi/letkf was used in this study as

225   the ETKF code library.

226

227   In many ensemble Kalman filter systems, the ensemble spread, $\boldsymbol{P^a}$, tends to become too

228   underdispersive to stably perform data assimilation cycles without any ensemble inflation

229   methods (Houtekamer and Zhang, 2016). To overcome this limitation, $\boldsymbol{P^a}$ is arbitrarily

230   inflated after data assimilation. In this paper, the relaxation to prior perturbation method

231   (RTPP) of Zhang et al. (2004) was used to maintain an appropriate ensemble spread. In

232   the RTPP, the computed analysis perturbations are relaxed back to the forecast

233   perturbations:

234    $x^a_{i,new} - \overline{x^a} = (1 - \alpha)(x^a_i - \overline{x^a}) + \alpha(x^f_i - \overline{x^f}),\ 0 \le \alpha \le 1$ (16)

235   where α was set to 0.975 in this study. If $\alpha = 1$, the analysis spread is identical to the

236   background spread. Many studies show that the ensemble inflation works well when α

237   remains fairly close to 1 (see also the comprehensive review by Houtekamer and Zhang

238   2016).

239

240   In the data assimilation experiments, I adjusted pressure head by data assimilation so that

241   x^f is pressure head. Since the surface saturated hydraulic conductivity was also adjusted,

242   x^f includes log-transformed $K_{s,surface}$. I assimilated volumetric soil moisture

243   observations so that y^f and y^o are simulated and observed volumetric soil moisture,

244   respectively. The van Genuchten relationship converts the adjusted state variables x^f to

245   the observable variables $\boldsymbol{y}^f$ and can be recognized as an observation operator $\mathcal{H}$.

246   However, since volumetric soil moisture $\boldsymbol{y}^f$ has already been calculated by Parflow, I did

247   not need the van Genuchten relationship in data assimilation.

248

249

250   **2.3. Kullback-Leibler divergence**

251   To evaluate the non-Gaussianity of the background error sampled by an ensemble, I used

252   the Kullback-Leibler divergence (KLD) (Kullback and Leibler 1951):

253     $D_{KL}(p, q) = \sum_i p(i) log \frac{p(i)}{q(i)}$ (17)

254   where $D_{KL}(p, q)$ is the KLD between two probabilistic distribution functions (PDFs), p

255   and q. If two PDFs are equal for all i, $D_{KL}(p, q) = 0$. A large value for $D_{KL}(p, q)$

256   indicates that the two PDFs, p and q, substantially differ from each other. Therefore,

257   the KLD can be used as an index to evaluate the closeness of two PDFs. In this study, I

258   compared the PDF of the ensemble simulation (p in equation (17)) with the Gaussian PDF

259   which has the mean and variance of the ensembles (q in equation (17)). A large value for

260     $D_{KL}(p, q)$ indicates the state variables simulated by ensembles do not follow the

261   Gaussian PDF. It should be noted that the KLD is not symmetric ($D_{KL}(p, q) \neq D_{KL}(q, p)$).

262   The KLD has been used to quantitatively evaluate the Gaussianity of the sampled

263 background error in the studies on data assimilation (e.g., Kondo and Miyoshi 2019; Duc

264 and Saito 2018).

265

266

267 **3. Synthetic experiments**

268 In this study, I performed two synthetic experiments. In the synthetic experiments, I

269 generated the synthetic truth of the state variables by driving ParFlow with the specified

270 parameters and input data. Then the synthetic observations were generated by adding the

271 Gaussian white noise to this synthetic truth. The performance of data assimilation was

272 evaluated by comparing the estimated state and parameter values by ETKF with the

273 synthetic truth. This synthetic experiment has been recognized as an important research

274 method to analyze how data assimilation works (e.g., Moradkhani et al. 2005; Camporese

275 et al. 2009; Vrugt et al. 2013; Kurtz et al. 2016; Sawada et al. 2018)

276

277

278 **3.1. Simple 2-D slope with homogeneous hydraulic conductivity**

279 **3.1.1. Experiment Design**

280   The synthetic experiment was implemented to examine how topography-driven surface

281   lateral flows contribute to efficiently propagating observation's information horizontally

282   in the data assimilation of soil moisture observation. Two synthetic reference runs were

283   created by Parflow. The 2-D domain has a horizontal extension of 4000m and a vertical

284   extension of 5m. The domain of the virtual slope was horizontally discretized into 40 grid

285   cells with a size of 100m and vertically discretized into 50 grid cells with a size of 0.10m.

286   The domain has a 25% slope. In two synthetic reference runs, it heavily rains only in the

287   upper half of the slope (2000m<x<4000m). Although this rainfall distribution is

288   unrealistic, the effect of surface lateral flows on data assimilation can clearly be discussed

289   in this simplified problem setting. More realistic rainfall distribution will be used in the

290   next synthetic experiment (see section 3.2). A constant rainfall rate of 50mm/h was

291   applied for 3 hours and then the period with no rainfall and evaporation of 0.075mm/h

292   lasted for 117 hours. This 120-hour rain/no rain cycle was repeatedly applied to the

293   domain. There is no rainfall in the lower half of the slope (0m<x<2000m). The

294   configurations described above were schematically shown in Figure 1a. The parameters

295   of the van Genuchten relationship, alpha and n, were set to 1.5 [m^{-1}] and 1.75, respectively.

296   Those values are in the reasonable range estimated by the published literature (e.g.,

297   Ghanbarian-Alavijeh et al. 2010). The porosity, ϕ in equation (1), was set to 0.40. The

298   Manning's coefficient, n_M in equation (5), was set to 5.52×10^{-6} [m$^{-1/3}$h]. These

299   clayey soil properties described above are applied to the whole domain. The groundwater

300   table was located at z=3m and the hydrostatic pressure gradient was assumed for the

301   initial pressure heads in the unsaturated soil layers.

302

303   The difference between two synthetic reference runs is the value of saturated hydraulic

304   conductivity. The surface saturated hydraulic conductivity, $K_{s,surface}$ in equation (3),

305   was set to 0.005 [m/h] in one reference, and 0.02 [m/h] in the other. These surface

306   saturated hydraulic conductivities described above are applied to the whole domain.

307   Figure 1 shows the difference of the response to heavy rainfall between the two synthetic

308   reference runs. In the case of the low saturated hydraulic conductivity (hereafter called

309   the LOW_K reference), larger surface lateral flows are generated than the case of the high

310   saturated hydraulic conductivity (hereafter called the HIGH_K reference). In the LOW_K

311   reference, the topography-driven surface lateral flows reach the left edge of the domain

312   (Figure 1b). In the HIGH_K reference, supplied water moves vertically rather than

313   horizontally and the topography-driven surface flow reaches around x = 1000~1500m

314   (Figure 1d).

315

316   For the data assimilation experiment, an ensemble of 50 realizations was generated. Each

317   ensemble member has different saturated hydraulic conductivity and rainfall rate.

318   Lognormal multiplicative noise was added to surface saturated hydraulic conductivity

319   and rainfall rate of the synthetic reference runs. This specification of uncertainty in

320   rainfall was also adopted in Crow et al. (2011). The two parameters of the lognormal

321   distribution, commonly called μ and σ, were set to 0 and 0.15, respectively. These

322   parameters were chosen to give the sufficiently large error in precipitation and saturated

323   hydraulic conductivity. In addition, this setting makes the rainfall PDF similar to the

324   Gaussian distribution, which is important to interpret the results of the experiments (see

325   the discussion section). The initial groundwater depth of each ensemble member was

326   drawn from the uniform distribution from 2.0m to 3.5m. The hydrostatic pressure gradient

327   was assumed for the initial pressure heads in the unsaturated soil layers.

328

329   The virtual hourly observations were generated by adding the Gaussian white noise whose

330   mean is zero to the volumetric soil moisture simulated by the synthetic reference runs.

331   The observation error (the standard deviation of the added Gaussian white noise) was set

332   to 0.05 m^3/m^3. It was assumed that the volumetric soil moistures can be observed in every

333   model's soil layer from surface to the depth of 1m at the specific location. These soil

334   moisture observations can be obtained in the in-situ observation sites (e.g., Dorigo et al.,

335   2017). In the section 3.2, I will assume that only surface soil moisture observation can be

336   accessed, which is more realistic since satellite sensors can observe only surface soil

337   moisture. I assumed that the small part of the domain can be observed. The two scenarios

338   of the observation's location are provided. In the first scenario (hereafter called the UP_O

339   scenario), the volumetric soil moisture at the upper part of the slope (x = 2500m) was

340   observed. In the UP_O scenario, I could observe the volumetric soil moisture in the upper

341   part of the slope where it heavily rains and tried to infer the soil moisture in the lower part

342   of the slope where it does not rain by propagating the observation's information downhill.

343   In the second scenario (hereafter called the DOWN_O scenario), the volumetric soil

344   moisture at the lower part of the slope (x = 1500m) was observed. In the DOWN_O

345   scenario, I could observe the volumetric soil moisture in the lower part of the slope where

346   it does not rain and tried to infer the soil moisture in the upper part of the slope where it

347   heavily rains by propagating the observation's information uphill.

348

349   Since I had the two synthetic reference runs (the HIGH_K and LOW_K references) and

350   the two observation scenarios (the UP_O and DOWN_O scenarios), I implemented totally

351   four data assimilation experiments. Table 1 summarizes the data assimilation experiments

352 implemented in this study. For instance, in the HIGH_K-UP_O experiment, I chose the

353 HIGH_K reference and generated an ensemble of 50 realizations from the HIGH_K

354 reference. The soil moisture observations were generated from the HIGH_K reference at

355 the location of x = 2500m and assimilated into the model every hour. The simulated

356 volumetric soil moisture of the data assimilation experiment was compared with that of

357 the HIGH_K reference.

358

359 In addition to the data assimilation (DA) experiments, I implemented the NoDA

360 experiment (also called the open-loop experiment in the literature of the LDAS study) in

361 which the ensemble was used but no observation data were assimilated. Please note that

362 in the NoDA experiment, the true rainfall rate and saturated hydraulic conductivity were

363 unknown so that I could not accurately estimate the synthetic true state variables. I will

364 evaluate how this negative impact of uncertainties in rainfall and saturated hydraulic

365 conductivity can be mitigated by data assimilation in the DA experiment.

366

367 As evaluation metrics, root-mean-square-error (RMSE) was used:

368 $\text{RMSE} = \sqrt{\frac{1}{k}\sum_{i=1}^{k}(F_i - T)^2}$ (18)

369   where k is the ensemble number, F_i is the volumetric soil moisture simulated by the i-th

370   member in the DA or NoDA experiment, T is the volumetric soil moisture simulated by

371   the synthetic reference run. I used all ensemble members to calculate RMSE because I

372   should evaluate not only if the ensemble mean is consistent to the synthetic truth, but also

373   if the extremely large ensemble spread simulated in the NoDA experiment is

374   appropriately reduced.

375

376   To evaluate the impact of data assimilation, the improvement rate (IR) was defined and

377   calculated by the following equation:

378    $IR = \frac{\overline{RMSE_{DA}} - \overline{RMSE_{NoDA}}}{\overline{RMSE_{NoDA}}}$ (19)

379   where $\overline{RMSE_{DA}}$ and $\overline{RMSE_{NoDA}}$ are time-mean RMSE of the DA and NoDA

380   experiments, respectively. The negative IR indicates that data assimilation positively

381   impacts the simulation of soil moisture. The metrics described above was calculated in

382   the whole domain. In the DA experiment, soil moisture values before the update by ETKF

383   (i.e. initial guess) were used to calculate the metrics.

384

385   Four of 120-hour rain/no rain cycles were applied so that the computation period was 480

386   hours. The spin-up results in the first 120 hours were not used to calculate the evaluation

387 metrics. Since the steady state of groundwater level is not the scope of this paper, the long

388 spin-up is not absolutely necessary.

389

390

391 **3.1.2. Results**

392 Figure 2a shows the IR of the LOW_K-UP_O experiment. The time series of the DA and

393 NoDA experiment and the synthetic reference run in the LOW_K-UP_O experiment can

394 be found in Figure S1. The data assimilation efficiently propagates the information of the

395 observations located in the upper part of the slope (see the black arrow in Figure 2a) both

396 horizontally and vertically. Despite the uncertainty in rainfall and hydraulic conductivity,

397 RMSE is reduced by data assimilation not only directly under the observation but also the

398 lower part of the slope where it does not rain. The estimated $K_{s,surface} \approx 0.00508$ [m/h]

399 by ETKF is mostly identical to the synthetic truth. However, the increase of RMSE by

400 data assimilation can be found at the left edge of the domain, which is far from the location

401 of the observation. The impact of data assimilation on the surface soil moisture simulation

402 is small because the volumetric soil moisture's RMSE of the NoDA experiment in this

403 surface soil layer is already small ($\leq 0.01 \text{m}^3/\text{m}^3$) in the case of the LOW_K reference so

404 that any improvements do not make sense.

405

406   Figure 2b shows the IR of the LOW_K-DOWN_O experiment (see also Figure S2 for

407   time series). The IR's spatial pattern of the LOW_K-DOWN_O experiment is similar to

408   that of the LOW_K-UP_O experiment except for the left edge of the domain. It is

409   promising that I can accurately infer soil moisture in the region where it heavily rains

410   from the shallow soil moisture observations in the region where it does not rain. The

411   estimated $K_{s,surface} \approx 0.00512$ [m/h] by ETKF is mostly identical to the synthetic truth.

412

413   Figure 3a shows the difference of time-mean RMSEs ($\overline{RMSE_{DA}}$ in equation (18))

414   between the LOW_K-UP_O and LOW_K-DOWN_O experiments. Although observing

415   the lower part of the slope slightly improves the soil moisture simulation at the left edge

416   of the domain compared with observing the upper part of the slope (the reason for it will

417   be explained later), there are few differences between the UP_O and DOWN_O scenarios

418   in the case of the LOW_K reference. The soil moisture observations have large

419   representativeness and I can efficiently infer soil moisture in the soil columns which are

420   horizontally and vertically far from the observations.

421

422   Figure 2c shows the IR of the HIGH_K-UP_O experiment (see also Figure S3 for time

423   series). The data assimilation significantly reduces RMSE of the soil moisture simulation

424   directly under the observations (see the black arrow in Figure 2c), which indicates that

425   the data assimilation efficiently propagates the information of the observations vertically.

426   The saturated hydraulic conductivity estimated by ETKF is mostly identical to the

427   synthetic truth ($K_{s,surface} \approx 0.0204$ [m/h]). However, the impact of the data assimilation

428   on the soil moisture simulation in the lower part of the slope around x=1500m is marginal

429   although there are large RMSE in the NoDA experiment ($>0.05m^3/m^3$) at the edge of the

430   area where topography-driven surface flow reaches in the HIGH_K reference (see Figure

431   1d).

432

433   Figure 2d shows the IR of the HIGH_K-DOWN_O experiment (see also Figure S4 for

434   time series). Although the observations in the lower part of the slope (see the black arrow

435   in Figure 2d) significantly contribute to improving the soil moisture simulation in the

436   downstream area of the observation and accurately estimating $K_{s,surface} \approx 0.0208$

437   [m/h], the impact of the data assimilation on the shallow soil moisture simulation around

438   x=500~1000m is marginal. As I found in the LOW_K-DOWN_O experiment, the shallow

439   soil moisture observations in the region where it does not rain can improve the soil

440   moisture simulation in the region where it heavily rains. However, the IR of the HIGH_K-

441   DOWN_O experiment in the upper part of the slope is smaller than that of the LOW_K-

442   DOWN_O experiment (see Figure 2b and 2d).

443

444   The high representativeness of the observations which I found in the case of the LOW_K

445   reference (i.e. the small difference of RMSEs between two observation scenarios) cannot

446   be found in the case of the HIGH_K reference. Figure 3b shows the difference of time-

447   mean RMSEs ($\overline{RMSE_{DA}}$ in equation (18)) between the HIGH_K-UP_O and HIGH_K-

448   DOWN_O experiments. Compared with the LOW_K reference case (Figure 3a), there

449   are significant differences between the UP_O and DOWN_O scenarios in the case of

450   higher saturated hydraulic conductivity. In this case, the vertical propagation of the

451   observations' information is more efficient than the horizontal propagation.

452

453   The relatively low efficiency of the data assimilation and the low representativeness of

454   the soil moisture observations in the case of the HIGH_K reference are caused by the

455   non-Gaussian background error distribution. I calculated KLD by comparing the PDF of

456   the NoDA ensemble (p in equation (17)) with the Gaussian PDF which has the mean and

457   variance of the NoDA ensemble (q in equation (17)). Figure 4 shows that the NoDA

458   ensemble in the case of the HIGH_K reference has stronger non-Gaussianity than the case

459   of the LOW_K reference especially in the shallow soil layers. The strong non-Gaussianity

460   of the NoDA ensemble generated from the HIGH_K reference can be found at the edge

461   of the area where the topography-driven surface flow reaches (Figure 1d). Figure 5 shows

462   that there is the bifurcation of the ensemble in this region when the ensemble is generated

463   from the HIGH_K reference. The process of topography-driven surface flows is switched

464   on if and only if the surface soil is saturated (see equation (6)) so that the ensemble tends

465   to be bifurcated into the members with surface flows and without surface flows. As I

466   mentioned in section 2.2, in the ETKF, the estimation of the state and parameter variables

467   is optimal if and only if the model's error has the Gaussian PDF and the relationship

468   between observed variables and unobserved variables is linear. Therefore, the non-

469   Gaussianity of the prior ensemble induced by the strong non-linear dynamics of surface

470   lateral flows makes the ETKF inefficient. It is more difficult to reconstruct 3-D fields of

471   soil moisture in high conductivity soils since the 1-D vertical water movement is more

472   dominant. The absolute RMSE of the NoDA experiment in the HIGH_K reference is

473   larger than the LOW_K reference in many places (not shown). Please note that the non-

474   Gaussianity can also be found in the LOW_K reference at the edge of the domain

475   (x=500m) due to the non-linear dynamics of surface lateral flows, which causes the

476   degradation of the soil moisture simulation in the LOW_K-UP_O experiment (see Figure

477   2a).

478

479

480   One of the major simplifications in this experiment is spatially homogeneous surface

481   saturated hydraulic conductivity. The optimization of it can efficiently improve the soil

482   moisture simulation in the whole domain. However, the optimization of this

483   homogeneous surface saturated hydraulic conductivity has a limited impact on the soil

484   moisture simulation. Figure S5 shows the IR of the HIGH_K-DOWN_O experiment

485   where the parameter optimization by ETKF is switched off. Even if I do not optimize the

486   surface saturated hydraulic conductivity, I could obtain the similar IR to the original

487   experiment and the shallow soil moisture observations in the region where it does not rain

488   can improve the soil moisture simulation in the region where it heavily rains. The

489   horizontal propagation of the observations' information shown in this experiment was

490   brought out not only by the estimation of spatially homogeneous saturated hydraulic

491   conductivity but also by the adjustment of state variables (i.e., pressure head and

492   volumetric soil moisture).

493

494   Please note that the improvement of the soil moisture simulation cannot be found if the

495   topography-driven surface flow is neglected. Figure S6 shows the IR of the LOW-

496   K_DOWN-O experiment where the topography-driven surface flow is neglected in the

497   ParFlow simulation. Please note that although many conventional land surface models

498   neglected or parameterized lateral flows, this assumption can be applied only in the coarse

499   spatial resolution (>25km), which is not the case of this experimental setting. The

500   imperfect model physics of ParFlow substantially degrades the skill to simulate soil

501   moisture and data assimilation cannot compensate this degradation. This point will also

502   be discussed in the section 3.2 more deeply.

503

504   3.2. Simple 3-D slope with heterogeneous hydraulic conductivity

505   3.2.1. Experiment design

506   To further demonstrate how land data assimilation works with topography-driven surface

507   lateral flows, I implemented another synthetic experiment which is more realistic than

508   that shown in section 3.1. The 3-D domain has a horizontal extension of 4000 m×4000m

509   and a vertical extension of 3m. The domain was horizontally discretized into 40×40 grid

510   cells with a size of 100m×100m and vertically discretized into 30 grid cells with a size

511   of 0.1m. The domain has a 10% slope in both x and y directions (see Figure 6a). The

512   parameters of the van Genuchten relationship, porosity and Manning's coefficient were

513   set to the same variables for the synthetic experiment in section 3.1.

514

515   The spatially heterogeneous surface saturated hydraulic conductivity was generated

516   following Kurtz et al. (2016). The field of $log_{10}(K_{s,surface})$ was generated by two-

517   dimensional unconditioned sequential Gaussian simulation. A Gaussian variogram with

518   nugget, sill, and range values of   0.0 $log_{10}(\text{m/h})$, 0.1 $log_{10}(m^2 h^2)$, and 12 model

519   grids (1200m), respectively was used to simulate the spatial distribution of

520   $log_{10}(K_{s,surface})$. A constant value of -2.30 $log_{10}(\text{m/h})$ (i.e. 0.005 (m/h)) was added

521   to the generated field so that the mean of the logarithm of surface saturated hydraulic

522   conductivity was set to -2.30 (i.e. 0.005(m/h)). This method to generate the field of the

523   saturated hydraulic conductivity has been used previously (e.g., Kurtz et al. 2016).

524   Subsurface saturated hydraulic conductivity was calculated by equation (3). An ensemble

525   of 51 realizations of $log_{10}(K_{s,surface})$ was generated and one of them was chosen as a

526   synthetic reference (Figure 6a). The remaining 50 members were used for data

527   assimilation experiments.

528

529   A rainfall rate $R(x, y)$ (mm/h) was modelled by a logistic function:

530     $R(x, y) = \frac{R_{max}}{1 + 100 \exp\left(-0.2 \times \frac{x+y}{2}\right)}$ (20)

531   where x and y are horizontal grid numbers ($1 \leq x \leq 40, 1 \leq y \leq 40$). In the synthetic

532   reference, the maximum rainfall rate in the domain, R_{max}, was set to 50 (mm/h) (Figure

533   6b). This rainfall rate was applied for 3 hours and then the period with no rainfall and

534   evaporation of 0.075mm/h lasted for 117 hours. For data assimilation experiment, an

535   ensemble of 50 realization of $R(x, y)$ was generated by adding a lognormal

536   multiplicative noise to R_{max} of the synthetic reference. The two parameters of the

537   lognormal distribution, commonly called μ and σ, were set to 0 and 0.15, respectively.

538

539   Figure 6c shows the distribution of surface soil moisture in the synthetic reference run.

540   Strong rainfall rate applied in the upper part of the slope generates the topography-driven

541   surface lateral flows. The virtual hourly observations were generated by adding the

542   Gaussian white noise, whose mean is zero and standard deviation is 0.05 m^3/m^3, to the

543   volumetric surface soil moisture simulated by the synthetic reference run. Unlike the

544   experiment in section 3.1, only surface soil moisture can be observed in this synthetic

545   experiment, which makes this experiment more realistic since satellite sensors can

546   observe only surface soil moisture. Three different observing networks with different

547   observation densities were used (Figure 7). The observing networks shown in Figure 7a,

548 7b, and 7c have totally 1, 9, and 361 observations and are called obs1, obs9, and obs361,

549 respectively.

550

551 In the DA experiments, those virtual observations of surface soil moisture were

552 assimilated every hour to adjust pressure head and saturated hydraulic conductivity. As I

553 did in the section 3.1, the NoDA experiments were also implemented. The two different

554 configurations of ParFlow were used for both DA and NoDA experiments. In the first

555 configuration, called OF (Overland Flow), Parflow explicitly solves overland flows. In

556 the second configuration, called noOF, Parflow assumes the flat terrain for surface flows

557 so that no overland flows are generated. Since the synthetic reference run explicitly

558 considers the topography-driven surface flow, the configuration of noOF assumes that the

559 model physics is imperfect. I implemented 8 numerical experiments which are

560 summarized in Table 2. For example, the OF_DA_obs9 experiment is the data

561 assimilation experiment with the observing network shown in Figure 7b, in which

562 Parflow explicitly solves the topography-driven surface flow. The noOF_NoDA is the

563 model run without assimilating observations, in which Parflow does not consider the

564 topography-driven surface flow.

565

3.2.2. Results

Figure 8a shows the RMSE of soil moisture simulation of a second soil layer (i.e. 10-20cm soil depth) in all 8 experiments (the same conclusion described below can be obtained by analyzing all of shallow soil layers). When Parflow explicitly solves the topography-driven surface flow, data assimilation substantially reduces RMSE of the soil moisture simulation (green bars in Figure 8a). The OF_DA_obs361 experiment has the smallest RMSE so that a denser observing network is beneficial to estimate soil moisture, although there is the stalled improvement from the OF_DA_obs1 experiment to the OF_DA_obs9 experiment (the reason for it will be explained later). Figure 8b shows the RMSE of the estimation of saturated surface hydraulic conductivity in all 8 experiments. Data assimilation also reduces the uncertainty in model's parameters (green bars in Figure 8b). However, the OF_DA_obs361 experiment has larger RMSE than the other DA experiments. This is because the adjustment of hydraulic conductivity in the OF_DA_obs361 experiment greatly mitigates not only the errors induced by uncertainty in hydraulic conductivity but those induced by uncertainty in rainfall rate. In the OF configuration, there are two sources of errors, rainfall rate and hydraulic conductivity. However, data assimilation can adjust only hydraulic conductivity in this study. Although

584   it is expected that the adjustment of hydraulic conductivity mainly mitigates the errors of

585   simulated volumetric soil moisture induced by uncertainty in hydraulic conductivity, it

586   also greatly mitigates those induced by uncertainty in rainfall rate by adjusting the

587   parameter in the incorrect direction when the number of observations is large. Therefore,

588   the assimilation of a large number of observations degrades the estimation of saturated

589   hydraulic conductivity despite the improvement of the soil moisture simulation.

590

591   The noOF_NoDA experiment has larger RMSE than the OF_NoDA experiment due to

592   the negligence of the topography-driven surface flow. In the noOF configuration, data

593   assimilation also improves the soil moisture simulation (red bars in Figure 8a). The

594   noOF_DA_obs361 experiment outperforms the OF_NoDA experiment so that data

595   assimilation with a dense observing network can compensate the negative impact of

596   neglecting the topography-driven surface flow. Although data assimilation positively

597   impacts the parameter estimation, the denser observing network cannot reduce RMSE of

598   hydraulic conductivity estimation (red bars in Figure 8b). The negative impact of the

599   dense observations in the noOF_DA_obs361 experiment on the parameter estimation is

600   larger than in the OF_DA_obs361 experiment. In addition to rainfall rate and hydraulic

601   conductivity, the imperfect model physics (i.e., no topography-driven surface flow) is the

602   source of error in the noOF configuration. The assimilation of a large number of

603   observations degrades the estimation of saturated hydraulic conductivity because it

604   greatly mitigates the impact of all systematic errors which comes from three different

605   sources only by adjusting hydraulic conductivity.

606

607   Figure 9 shows the difference of RMSE of the soil moisture simulation between the DA

608   experiments and the OF_NoDA experiment. In the DA configuration, the improvement

609   of the soil moisture estimation can be found in a large area even if there is a single

610   observation in the center of the domain (Figure 9a). Figure 9b shows that the increase of

611   the number of observations substantially improves the soil moisture simulation in the

612   region which is affected by topography-driven surface flow (see also Figure 6c). However,

613   the skill to simulate soil moisture is severely degraded in the lower-left corner of the

614   domain, which causes the stalled improvement from the OF_DA_obs1 experiment to the

615   OF_DA_obs9 experiment shown in Figure 8a. Figure 9c shows that although the far

616   denser observing network can slightly mitigate this degradation, increasing the number

617   of observations cannot efficiently solve this issue. This degradation is caused by the

618   bifurcation of ensemble members at the edge of the area where topography-driven surface

619   flow reaches (Figure S7). Figure 10 shows KLD in the OF_NoDA and noOF_NoDA

620   experiments. Figure 10a clearly shows that the ensemble simulation of volumetric soil

621   moisture generates the strong non-Gaussianity at the edge of the area where topography-

622   driven surface flow reaches, which harms the efficiency of the ETKF. This finding is

623   consistent to what I found in the previous experiment in section 3.1.

624

625   In the noOF configuration, there are large errors in the area around 500<=x, y <=1500

626   (not shown) since the increase of soil moisture in this area is caused by the topography-

627   driven surface flow which is neglected in the noOF configuration. Figures 9d and 9e show

628   that the sparse observations cannot completely remove this degradation caused by

629   imperfect model physics. Figure 9f shows that the noOF_DA_obs361 can outperform the

630   OF_NoDA experiment in exchange for the degradation of the parameter estimation as I

631   found in Figure 8. The unstable behavior of the ETKF found in the OF configuration does

632   not occur when the topography-driven surface flow is neglected since the ensemble

633   simulation does not generate the non-Gaussian background distribution (Figure 10b).

634   Although ETKF can significantly improve the simulation skill of the hyperresolution land

635   model in many cases, I found its limitation when it is applied to the problems with the

636   topography-driven surface lateral flows. Figure 10 clearly indicates that this limitation

637   appears only if lateral water flows are explicitly considered.

638

639

640

4. Discussion

In this study, I revealed that the hyperresolution integrated surface-subsurface

hydrological model gives the unique opportunity to effectively use soil moisture

observations to improve the soil moisture simulation in terms of a horizontal propagation

of observation's information in a model space. I found that the explicit calculation of the

topography-driven surface flow has an important role in propagating the information of

soil moisture observation horizontally by data assimilation even if there is considerable

heterogeneity of meteorological forcing. It is possible that the soil moisture observations

in the area where it does not heavily rain can improve the soil moisture simulation in the

severe rainfall area.

651

This potential cannot be brought out in the conventional 1-D LSM where sub-grid scale

surface runoff is parameterized and the surface flows in one grid do not move to the

adjacent grids. I found that neglecting the topography-driven surface flow causes

significant bias in the soil moisture simulation and this bias cannot be completely

656   mitigated by data assimilation especially in the case of a sparse observing network.

657   However, I found that even if the model uses imperfect physics which neglects the

658   interaction between topography-driven surface lateral flows and subsurface soil moisture,

659   assimilating soil moisture observations into the model's three-dimensional state and

660   parameter space can improve the skill to estimate soil moisture and hydraulic conductivity.

661   This finding implies that the conventional 1-D LSM with full 3-D data assimilation may

662   be a computationally cheap and reasonable choice in some cases although many land data

663   assimilation systems with the conventional 1-D LSM currently update state variables only

664   in a single model's horizontal grid which is identical to the location of the observation.

665

666   The conventional ensemble data assimilation (i.e. ETKF) severely suffers from the non-

667   Gaussian background error PDFs caused by the strongly nonlinear dynamics of the

668   topography-driven surface flow although it has been widely used by previous studies (e.g.,

669   Camporese et al. (2009); Camporese et al. (2010); Ridler et al. (2014); Zhang et al. (2015);

670   Kurtz et al. (2016); Zhang et al. (2018)). The efficiency of ETKF to propagate the

671   information of observations horizontally in the model space is limited in the edge of the

672   area where the topography-driven surface flow reaches. Please note that the low

673   representativeness of the soil moisture observations in the case of the HIGH_K reference

674 shown in section 3.1 is due to the limitation of the Kalman filter that the error PDFs need

675 to follow the Gaussian distribution to get the optimal estimation so that the increase of

676 the ensemble size cannot solve this issue. I implemented the data assimilation experiment

677 in the case of the HIGH_K reference with an ensemble size of 500, which is 10 times

678 larger than the original experiments shown in section 3.1, and found no significant

679 improvement of the soil moisture simulation (not shown). Some studies revealed that

680 volumetric soil moisture distributions follow the Gaussian distribution better than

681 pressure head so that they recommend updating soil moisture as a state variable (e.g.,

682 Zhang et al. (2018)). However, in this study, I found that volumetric soil moisture

683 distributions have bimodal structure and do not follow the Gaussian distribution. The

684 limitation of ensemble Kalman filters found in this study does not depend on the updated

685 state variables.

686

687 In addition, I found ensemble clustering in which the ensemble members are split into a

688 single outlier and the others (see Figures S1-S4). The previous studies found that this

689 ensemble clustering is generated by the non-Gaussian PDF (Anderson 2010; Amezcua et

690 al. 2012). Ensemble clustering shown in the analysis timeseries also implies that the non-

691   Gaussian PDF plays an important role in the data assimilation of the hyperresolution land

692   model.

693

694

695   The spatially dense soil moisture observations are needed to efficiently constrain state

696   variables at the edge of surface flows. High resolution soil moisture remote sensing based

697   on satellite active and passive combined microwave observations at the 1 km spatial

698   resolution (e.g., He et al. 2018) and the assimilation of those data (Lievens et al. 2017)

699   may be important in the era of the hyperresolution land modeling. High resolution

700   observations of surface inundated water from satellite imagery with a spatial resolution

701   finer than 100 m (e.g., Sakamoto et al. 2007; Arnesen et al. 2013) may also be useful.

702   However, the numerical experiment in section 3.2 implies that the dense observing

703   network of surface soil moisture cannot completely remove the negative impact of the

704   non-Gaussian background PDF.

705

706   As a possible heuristic approach to avoid the negative impact of the non-Gaussian

707   background PDF, I can omit to update the state variables in the edge of the area where

708   topography-driven surface flow reaches. The numerical experiments clearly indicate that

709   the negative impact of the non-linear physics and non-Gaussian PDF is found only in the

710   edge of flooding areas so that it is beneficial to simply omit to update the state variables

711   in this area. It is similar but not conceptually identical to the localization method, in which

712   the spurious correlation sampled by an ensemble is eliminated by spatially restricting the

713   impact of assimilating observation (e.g., Rasmussen et al. 2015; Anderson 2007; Bishop

714   and Hodyss 2009).

715

716   Reducing the uncertainty in rainfall positively impacts the efficiency of data assimilation

717   since the bifurcation of simulated soil moisture found in Figure 5c is originally induced

718   by the uncertainty in rainfall. Although assimilating land hydrological observations to

719   improve the rainfall input has been intensively investigated (e.g., Sawada et al. 2018;

720   Herrnegger et al. 2015; Crow et al. 2011; Vrugt et al. 2008), it has yet to be applied to

721   hyperresolution land models. Please note that the parameters of the lognormal distribution

722   to model the uncertainty in rainfall were specified to make the rainfall PDF similar to the

723   Gaussian distribution. I chose the lognormal distribution in order not to generate negative

724   rainfall values and I intended not to introduce non-Gaussianity into the external forcing.

725   The rainfall input which follows the Gaussian PDF was transformed into the non-

726   Gaussian PDF of the background error by the strongly nonlinear dynamics of the

727   topography-driven surface flow.

728

729   To explicitly consider non-Gaussianity and non-linear relationship between observed and

730   unobserved variables induced by the topography-driven surface flow, the particle filters

731   may be useful. The particle filter can represent a probability distribution (including non-

732   Gaussian distributions) directly by an ensemble. Particle filters have been intensively

733   applied to conventional 1-D LSMs (e.g., Sawada et al. 2015; Qin et al. 2009) and lumped

734   hydrological models (e.g., Yan and Moradkhani 2016; Vrugt et al. 2013). Although

735   particle filtering in a high dimensional system suffers from the "curse of dimensionality"

736   (e.g., Snyder et al. 2008), some studies developed the methodology to improve the

737   efficiency of particle filtering (e.g., van Leeuwen 2009; Poterjoy et al. 2019). The

738   applicability of particle filtering to 3-D hyperresolution land models should be assessed

739   in the future.

740

741   Since the synthetic numerical experiments in this paper adopted the simple and

742   minimalistic setting, the findings of this paper may be exaggerated. There are no river

743   channels in the synthetic experiment so that the skill to simulate river water level and

744 discharge cannot be discussed, which is the major limitation of this study. The simple

745 representation of soil properties is also a limitation of this study. Although the prior

746 uncertainty in rainfall and saturated hydraulic conductivity was arbitrary chosen in this

747 study, the specification of the prior knowledge is not straightforward in the real-world

748 applications. In future work, the contributions of the topography-driven surface runoff

749 process to the data assimilation of hydrological observations should be quantified in real-

750 world applications. In addition, in the virtual experiment of this paper, I neglected some

751 of the important land processes such as transpiration, canopy interception, snow, and

752 frozen soil. These processes affect the source term of equation (1) in hyper-resolution

753 land models (e.g., Shrestha et al. 2014). Since the inclusion of the neglected processes do

754 not change the structure of the original ParFlow, the findings of this study can be robust

755 to the models which include these processes. Although they are generally not primary

756 factors in the propagation of overland flows generated by extreme rainfall, which has a

757 shorter timescale than the neglected processes, those processes should be considered in

758 the future.

759

760 The other limitation of this study is that I could not thoroughly evaluate the skill of the

761 ensemble data assimilation to quantify the uncertainty of its prediction. Following

762   Abbazadeh et al. (2019), I calculated the 95% exceedance ratio and found that the

763   ensemble forecast was systematically overconfident (not shown). In the synthetic

764   experiments of this study, the number of rainfall events was small, and the timing and

765   magnitude of rainfall were not diversified. Due to this limited amount of data, it is difficult

766   to deeply discuss the accuracy of the quantified uncertainty by data assimilation. While

767   the skill of lumped hydrological models was often evaluated by the probabilistic

768   performance measures such as the 95% exceedance ratio (e.g., Abbazadeh et al. (2019)),

769   the uncertainty quantification of the simulation of hyper-resolution land models is in its

770   infancy. How surface lateral flows affect the accuracy of the uncertainty quantification by

771   data assimilation should be investigated using more realistic data.

772

773

774   **5. Conclusions**

775   The simplified synthetic experiments of this study indicate that topography-driven lateral

776   surface flows induced by heavy rainfalls do matter for data assimilation of hydrological

777   observations into hyperresolution land models. Even if there is extreme heterogeneity of

778   rainfall, the information of soil moisture observations can be propagated horizontally in

779   the model space and the soil moisture simulation can be improved by the ensemble

780   Kalman filter. However, the nonlinear dynamics of the topography-driven surface flow

781   induces the non-Gaussianity of the model error, which harms the efficiency of data

782   assimilation of soil moisture observations. It is difficult to efficiently constrain model

783   states at the edge of the area where the topography-driven surface flow reaches by linear-

784   Gaussian filters, which brings the new challenge in land data assimilation for

785   hyperresolution land models. Future work will focus on the real-world applications using

786   intense in-situ soil moisture observation networks and/or high-resolution satellite soil

787   moisture observations.

788

789

790   **Acknowledgement**

791   This study was supported by the JSPS KAKENHI grant JP17K18352 and JP18H03800.

792   I thank two anonymous reviewers for their constructive comments.

793

794   **Code/Data Availability**

795   All data used in this paper are stored in the repository of the University of Tokyo for 5

796   years and available upon request to the author. The ETKF code used in this study can be

797   found at https://github.com/takemasa-miyoshi/letkf.

798

Author Contribution

YS designed the study, executed numerical experiments, analyzed the results, and wrote

the paper.

802

Competing interests

The author declares no competing interests.

805

References

807

Abbaszadeh, P., Moradkhani, H., and Daescu, D., N.: The Quest for Model Uncertainty

Quantification: A Hybrid Ensemble and Variational Data Assimilation Framework. *Water*

Resources Research, 55, 2407– 2431. https://doi.org/10.1029/2018WR023629, 2019.

811

Ait-El-Fquih, B., El Gharamti, M., and Hoteit, I.: A Bayesian consistent dual ensemble

Kalman filter for state-parameter estimation in subsurface hydrology. *Hydrology and*

Earth System Sciences, *20*(8), 3289–3307. https://doi.org/10.5194/hess-20-3289-2016,

2016

816

Amesen et al.: Monitoring flood extent in the lower Amazon River floodplain using

ALOS/PALSAR ScanSAR images. *Remote Sensing of Environment, 130,* 51-61.

https://doi.org/10.1016/j.rse.2012.10.035, 2013

820

Amezcua, J., Ide, K., Bishop, C. H., and Kalnay, E.: Ensemble clustering in deterministic

ensemble Kalman filters, *Tellus, 64A,* 1-12, https://doi.org/10.3402/tellusa.v64i0.18039,

2012.

824

Anderson, J. L.: Exploring the need for localization in ensemble data assimilation using

a hierarchical ensemble filter. *Physica D: Nonlinear Phenomena*, *230*(1–2), 99–111.

https://doi.org/10.1016/j.physd.2006.02.011, 2007

828

Anderson, J. L.: A non-Gaussian ensemble filter update for data assimilation*, Mon. Wea.

Rev., 138,* 4186-4198, https://doi.org/10.1175/2010MWR3253.1, 2010.

831

832 Bandara, R., Walker, J. P., and Rüdiger, C.: Towards soil property retrieval from space:

833 Proof of concept using in situ observations. *Journal of Hydrology, 5*12, 27–38.

834 https://doi.org/10.1016/j.jhydrol.2014.02.031, 2014

835

836 Bandara, R., Walker, J. P., Rüdiger, C., and Merlin, O.: Towards soil property retrieval

837 from space: An application with disaggregated satellite observations. *Journal of*

838 *Hydrology, 522,* 582-593, https://doi.org/10.1016/j.jhydrol.2015.01.018, 2015

839

840 Beven, K.: On subsurface stormflow: an analysis of response times, *Hydrological Science*

841 *Journal, 27,* 505-521, doi:10.1080/02626668209491129, 1982

842

843 Bishop, C.H., Etherton, B., J., and Majumdar, S., J.: Adaptive Sampling with the

844 Ensemble Transform Kalman Filter. Part I: Theoretical Aspects. *Monthly. Weather.*

845 *Review.,* ***129***, 420–436, https://doi.org/10.1175/1520-

846 0493(2001)129<0420:ASWTET>2.0.CO;2, 2001.

847

848 Bishop, C. H., and Hodyss, D.: Ensemble covariances adaptively localized with ECO-

849 RAP. Part 1: Tests on simple error models. *Tellus, 61A,* 84–96,

850 https://doi.org/10.1111/j.1600-0870.2008.00371.x, 2009.

851

852 Camporese, M., Paniconi, C., Putti, M., and Salandin, P.: Ensemble Kalman filter data

853 assimilation for a process-based catchment scale model of surface and subsurface flow.

854 *Water Resources Research*, *45*(10), 1–14. https://doi.org/10.1029/2008WR007031, 2009.

855

856 Camporese, M., Paniconi, C., Putti, M., and Orlandini, S.: Surface-subsurface flow

857 modeling with path-based runoff routing, boundary condition-based coupling, and

858 assimilation of multisource observation data. *Water Resources Research*, *46*(2).

859 https://doi.org/10.1029/2008WR007536, 2010.

860

861 Crow, W. T., Van Den Berg, M. J., Huffman, G. J., and Pellarin, T.: Correcting rainfall

862 using satellite-based surface soil moisture retrievals: The Soil Moisture Analysis Rainfall

863 Tool (SMART). *Water Resources Research*, *47*(8), 1–15.

864 https://doi.org/10.1029/2011WR010576, 2011.

865

866   Dorigo et al.: ESA CCI Soil Moisture for improved Earth system understanding: State-

867   of-the art and future directions, *Remote Sensing of Environment, 203,* 185-215,

868   https://doi.org/10.1016/j.rse.2017.07.001, 2017

869

870   Duc, L., and Saito, K.: Verification in the presence of observation errors: Bayesian point

871   of view. *Q. J. R. Meteorol. Soc., 144,* 1063– 1090. https://doi.org/10.1002/qj.3275, 2018.

872

873   Fang, Y., L. R. Leung, Z. Duan, M. S. Wigmosta, R. M. Maxwell, J. Q. Chambers, and J.

874   Tomasella: Influence of landscape heterogeneity on water available to tropical forests in

875   an Amazonian catchment and implications for modeling drought response, *J. Geophys.*

876   *Res. Atmos., 122,* https://doi.org/10.1002/2017JD027066, 2017.

877

878   Ghanbarian-Alavijeh, B., Liaghat, A., Huang, G., H., and van Genuchten, M. Th.,:

879   Estimation of the van Genuchten soil water retention properties from soil textural data.

880   *Pedosphere. 20(4)*: 456–465., 2010

881

882   Han, X., Franssen, H.-J. H., Montzka, C. and Vereecken, H.: Soil moisture and soil

883   properties estimation in the Community Land Model with synthetic brightness

884   temperature   observations,   *Water   Resources   Research.,   50,*   6081 – 6105,

885   https://doi.org/10.1002/2013WR014586, 2014

886

887   Herrnegger, M., Nachtnebel, H. P., and Schulz, K.: From runoff to rainfall : inverse

888   rainfall   –   runoff   modelling   in   a   high   temporal   resolution,   4619–4639.

889   https://doi.org/10.5194/hess-19-4619-2015, 2015

890

891   He, L., Hong, Y., Wu, X., Ye, N., Walker, J. P. and Chen, X.: Investigation of SMAP

892   Active–Passive Downscaling Algorithms Using Combined Sentinel-1 SAR and SMAP

893   Radiometer Data. *IEEE Transactions on Geosciences and Remote Sensing, 56,* 4906-

894   4918, https://doi.org/10.1109/TGRS.2018.2842153, 2018

895

896   Hendricks Franssen, H. J., and Kinzelbach, W.: Real-time groundwater flow modeling

897   with the Ensemble Kalman Filter: Joint estimation of states and parameters and the filter

898   inbreeding   problem.   *Water   Resources   Research,   44*(9),   1–21.

899   https://doi.org/10.1029/2007WR006505, 2008

900

901 Houborg, R., Rodell, M., Li, B., Reichle, R., and Zaitchik, B. F.: Drought indicators based

902 on model-assimilated Gravity Recovery and Climate Experiment (GRACE) terrestrial

903 water storage observations. *Water Resources Research*, *48*(7).

904 https://doi.org/10.1029/2011WR011291, 2012

905

906 Houtekamer, P. L., and Zhang, F.: Review of the Ensemble Kalman Filter for Atmospheric

907 Data Assimilation. *Monthly Weather Review*, MWR-D-15-0440.1.

908 https://doi.org/10.1175/MWR-D-15-0440.1 , 2016

909

910 Hunt, B. R., Kostelich, E. J., and Szunyogh, I.: Efficient data assimilation for

911 spatiotemporal chaos: A local ensemble transform Kalman filter. *Physica D: Nonlinear*

912 *Phenomena*, *230*(1–2), 112–126. https://doi.org/10.1016/j.physd.2006.11.008, 2007

913

914 Ji, P., Yuan, X., and Liang, X. Z.: Do Lateral Flows Matter for the Hyperresolution Land

915 Surface Modeling? *Journal of Geophysical Research: Atmospheres*, 1–16.

916 https://doi.org/10.1002/2017JD027366, 2017

917

918   Keune, J., F. Gasper, K. Goergen, A. Hense, P. Shrestha, M. Sulis, and S. Kollet: Studying

919   the influence of groundwater representations on land surface-atmosphere feedbacks

920   during the European heat wave in 2003, *Journal of Geophysical Research. Atmospheres*,

921   121, 13,301–13,325, https://doi.org/10.1002/2016JD025426, 2016.

922

923   Kollet, S. J., and Maxwell, R. M.: Integrated surface–groundwater flow modeling: A free-

924   surface overland flow boundary condition in a parallel groundwater flow model.

925   *Advances   in   Water   Resources*,   *29*(7),   945–958.

926   https://doi.org/10.1016/j.advwatres.2005.08.006, 2006.

927

928   Kondo, K., and Miyoshi, T.: Non-Gaussian statistics in global atmospheric dynamics: a

929   study with a 10 240-member ensemble Kalman filter using an intermediate atmospheric

930   general   circulation   model.   *Nonlinear   Processes   in   Geophysics,   26,*   211-225.

931   https://doi.org/10.5194/npg-26-211-2019, 2019

932

933   Kumar, S. V., Reichle, R. H., Koster, R. D., Crow, W. T., and Peters-Lidard, C. D.: Role

934   of Subsurface Physics in the Assimilation of Surface Soil Moisture Observations. *Journal*

935   *of Hydrometeorology, 10*(6), 1534–1547. https://doi.org/10.1175/2009JHM1134.1, 2009

936

937 Kurtz, W., He, G., Kollet, S. J., Maxwell, R. M., Vereecken, H., and Franssen, H. J. H.:

938 TerrSysMP-PDAF (version 1.0): A modular high-performance data assimilation

939 framework for an integrated land surface-subsurface model. *Geoscientific Model*

940 *Development*, *9*(4), 1341–1360. https://doi.org/10.5194/gmd-9-1341-2016, 2016.

941

942 Kullback, S., and Leibler, R. A.: On information and sufficiency, *The Annals of*

943 *Mathematical Statistics, 22*, 79-86, 1951.

944

945 Lawrence, D. M., et al.: Parameterization improvements and functional and structural

946 advances in Version 4 of the Community Land Model. *Journal of Advances in Modeling*

947 *Earth Systems*, *3*(3), 1–27. https://doi.org/10.1029/2011MS000045, 2011

948

949 Li, B., Rodell, M., Zaitchik, B. F., Reichle, R. H., Koster, R. D., and van Dam, T. M.:

950 Assimilation of GRACE terrestrial water storage into a land surface model: Evaluation

951 and potential value for drought monitoring in western and central Europe. *Journal of*

952 *Hydrology*, *446–447*, 103–115. https://doi.org/10.1016/j.jhydrol.2012.04.035, 2012

953

954 Lievens, et al.: Joint Sentinel-1 and SMAP data assimilation to improve soil moisture

955 estimates. *Geophysical Research Letters*, *44*(12), 6145–6153.

956 https://doi.org/10.1002/2017GL073904, 2017.

957

958 Martens, B., Miralles, D. G., Lievens, H., Schalie, R. Van Der, and Jeu, R. A. M. De.:

959 GLEAM v3 : satellite-based land evaporation and root-zone soil moisture, *Geoscientific*

960 *Model Development, 10,* 1903–1925. https://doi.org/10.5194/gmd-10-1903-2017, 2017

961

962 Maxwell, R. M., and N. L. Miller: Development of a Coupled Land Surface and

963 Groundwater Model. *Journal of Hydrometeorology, 6,* 233-247.

964 https://doi.org/10.1175/JHM422.1, 2005

965

966 Maxwell, R. M., and Condon, L. E.: Connections between groundwater flow and

967 transpiration partitioning. *Science, 353*, 377-380, https://doi.org/10.1126/science.aaf7891,

968 2016

969

970 Maxwell, R. M., Condon, L. E., and Kollet, S. J.: A high-resolution simulation of

971 groundwater and surface water over most of the continental US with the integrated

972 hydrologic model ParFlow v3, 923–937. https://doi.org/10.5194/gmd-8-923-2015, 2015.

973

974 Maxwell, R. M., and Kollet, S. J.: Interdependence of groundwater dynamics and land-

975 energy feedbacks under climate change, *Nature Geoscience, 1,* 665–669.

976 https://doi.org/10.1038/ngeo315, 2008.

977

978 Maxwell, R. M., Lundquist, J. K., Mirocha, J. D., Smith, S. G., Woodward, C. S., and

979 Tompson, A. F. B.: Development of a Coupled Groundwater–Atmosphere Model.

980 *Monthly Weather Review*, *139*(1), 96–116. https://doi.org/10.1175/2010MWR3392.1,

981 2011

982

983 Moradkhani, H., Hsu, K. L., Gupta, H., and Sorooshian, S.: Uncertainty assessment of

984 hydrologic model states and parameters: Sequential data assimilation using the particle

985 filter. *Water Resources Research, 41(5)*, 1–17. https://doi.org/10.1029/2004WR003604,

986 2005

987

988 Nerger, L., and Hiller, W.,: Software for ensemble-based data assimilation systems –

989 implementation strategies and scalability. *Computers and Geosciences. 55,* 110–118.

990 https://doi.org/10.1016/j.cageo.2012.03.026, 2013

991

992 Niu, G. Y., Paniconi, C., Troch, P. a., Scott, R. L., Durcik, M., Zeng, X., and Goodrich, D.

993 C.: An integrated modelling framework of catchment-scale ecohydrological processes: 1.

994 Model description and tests over an energy-limited watershed. *Ecohydrology*, *7*(2), 427–

995 439. https://doi.org/10.1002/eco.1362, 2014

996

997 Paloscia, S, Pettinato, S., Santi, E., Notarnicola, C., Pasolli, L., and Reppucci, A.: Soil

998 moisture mapping using Sentinel-1 images: Algorithm and preliminary validation.

999 *Remote Sensing of Environment, 134,* 234-248. https://doi.org/10.1016/j.rse.2013.02.027,

1000 2013.

1001

1002 Pokhrel, P., and Gupta, H. V.: On the use of spatial regularization strategies to improve

1003 calibration of distributed watershed models. *Water Resources Research*, *46*(1), 1–17.

1004 https://doi.org/10.1029/2009WR008066, 2010

1005

1006 Poterjoy, J., Wicker, L., and Buehner, M.: Progress toward the application of a localized

1007 particle filter for numerical weather prediction. *Monthly Weather Review, 147(4)*, 1107–

1008 1126. https://doi.org/10.1175/MWR-D-17-0344.1, 2019

1009

1010 Qin, J., Liang, S., Yang, K., Kaihotsu, I., Liu, R., and Koike, T.: Simultaneous estimation

1011 of both soil moisture and model parameters using particle filtering method through the

1012 assimilation of microwave signal. *Journal of Geophysical Research*, *114*(D15), 1–13.

1013 https://doi.org/10.1029/2008JD011358, 2009.

1014

1015 Rasmussen, J., Madsen, H., Jensen, K. H., and Refsgaard, J. C.: Data assimilation in

1016 integrated hydrological modeling using ensemble Kalman filtering: evaluating the effect

1017 of ensemble size and localization on filter performance. *Hydrology and Earth System*

1018 *Sciences*, *19*(7), 2999–3013. https://doi.org/10.5194/hess-19-2999-2015, 2015.

1019

1020 Ridler, M.-E., H. Madsen, S. Stisen,, S. Bircher, and R. Fensholt, Assimilation of SMOS-

1021 derived soil moisture in a fully integrated hydrological and soil-vegetation-atmosphere

1022 transfer model in Western Denmark, *Water Resour. Res., 50,* 8962 – 8981,

1023 https://doi.org/10.1002/2014WR015392, 2014.

1024

1025 Sakamoto, T., et al.: Detecting temporal changes in the extent of annual flooding within

1026 the Cambodia and the Vietnamese Mekong Delta from MODIS time-series imagery.

1027 *Remote Sensing of Environement, 109,* 295-313.

1028 https://doi.org/10.1016/j.rse.2007.01.011, 2007.

1029

1030 Sawada, Y. and Koike, T.: Simultaneous estimation of both hydrological and ecological

1031 parameters in an eco-hydrological model by assimilating microwave signal, *Journal of*

1032 *Geophysical Research – Atmospheres, 119,* 8839-8857,

1033 https://doi.org/10.1002/2014JD021536, 2014.

1034

1035 Sawada, Y., Koike, T., and Walker, J. P.: A land data assimilation system for simultaneous

1036 simulation of soil moisture and vegetation dynamics, *Journal of Geophysical Research –*

1037 *Atmospheres*, *120,* 5910-5930, https://doi.org/10.1002/2014JD022895, 2015

1038

1039 Sawada, Y., Nakaegawa, T, and Miyoshi, T.: Hydrometeorology as an inversion problem:

1040 Can river discharge observations improve the atmosphere by ensemble data assimilation?,

1041 *Journal of Geophysical Research - Atmospheres, 123*, 848-860,

1042 https://doi.org/10.1002/2017JD027531, 2018

1043

1044 Sellers, P. J., et al.: A revised land surface parameterization (SiB2) for atmospheric GCMs.

1045 Part I: Model formulation. *Journal of Climate.* https://doi.org/10.1175/1520-

1046 0442(1996)009<0676:ARLSPF>2.0.CO;2, 1996

1047

1048 Shrestha, P., Sulis, M., Masbou, M., Kollet, S., and Simmer, C.: A Scale-Consistent

1049 Terrestrial Systems Modeling Platform Based on COSMO, CLM, and ParFlow. *Monthly*

1050 *Weather Review*, *142*(9), 3466–3483. https://doi.org/10.1175/MWR-D-14-00029.1, 2014

1051

1052 Snyder, C., Bengtsson, T., Bickel, P., and Anderson, J.: Obstacles to High-Dimensional

1053 Particle Filtering. *Monthly Weather Review*, *136*(12), 4629–4640.

1054 https://doi.org/10.1175/2008MWR2529.1, 2008

1055

1056 Tian, W., Li, X., Cheng, G. D., Wang, X. S., and Hu, B. X.: Coupling a groundwater

1057 model with a land surface model to improve water and energy cycle simulation.

1058 *Hydrology and Earth System Sciences*, *16*(12), 4707–4723. https://doi.org/10.5194/hess-

1059 16-4707-2012, 2012.

1060

1061 Van Genuchten, M. T.: A closed-form equation for predicting the hydraulic conductivity

1062 of unsaturated soils, *Soil Science Society of America Journal*, *44*, 892–898, 1980.

1063

1064 Van Leeuwen, P., J.: Particle Filtering in Geophysical Systems, *Monthly Weather Review,*

1065 *137,* 4089-4114, https://doi.org/10.1175/2009MWR2835.1, 2009

1066

1067 Verbeeck, H., Peylin, P., Bacour, C., Bonal, D., Steppe, K., and Ciais, P.: Fluxes in

1068 Amazon forests: Fusion of eddy covariance data and the ORCHIDEE model. Journal of

1069 Geophysical Research, 116(G2), 1–19. https://doi.org/10.1029/2010JG001544, 2011.

1070

1071 Vrugt, J. A., ter Braak, C. J. F., Clark, M. P., Hyman, J. M., and Robinson, B. A.:

1072 Treatment of input uncertainty in hydrologic modeling: Doing hydrology backward with

1073 Markov chain Monte Carlo simulation. *Water Resources Research*, *44*, 1–15.

1074 https://doi.org/10.1029/2007WR006720, 2008.

1075

1076 Vrugt, J. A., ter Braak, C. J. F., Diks, C. G. H., and Schoups, G.: Hydrologic data

1077 assimilation using particle Markov chain Monte Carlo simulation: Theory, concepts and

1078 applications. *Advances in Water Resources*, *51*, 457–478.

1079 https://doi.org/10.1016/j.advwatres.2012.04.002, 2013.

1080

1081 Williams, J. L., and Maxwell, R. M.: Propagating Subsurface Uncertainty to the

1082 Atmosphere Using Fully Coupled Stochastic Simulations. *Journal of Hydrometeorology*,

1083 *12*(4), 690–701. https://doi.org/10.1175/2011JHM1363.1, 2011.

1084

1085 Wood, E. F., et al.: Hyperresolution global land surface modeling : Meeting a grand

1086 challenge for monitoring Earth's terrestrial water, *Water Resources Research, 47*,

1087 https://doi.org/10.1029/2010WR010090, 2011.

1088

1089 Yan, H., and Moradkhani, H.: Combined assimilation of streamflow and satellite soil

1090 moisture with the particle filter and geostatistical modeling. *Advances in Water Resources*,

1091 *94*, 364–378. https://doi.org/10.1016/j.advwatres.2016.06.002, 2016.

1092

1093 Yang, K., Koike, T., Kaihotsu, I., and Qin, J.: Validation of a Dual-Pass Microwave Land

1094 Data Assimilation System for Estimating Surface Soil Moisture in Semiarid Regions.

1095 *Journal of Hydrometeorology*, *10*(3), 780–793. https://doi.org/10.1175/2008JHM1065.1,

1096 2009.

1097

1098 Yang, K., Watanabe, T., Koike, T., Li, X., Fujii, H., Tamagawa, K., and Ishikawa, H.:

1099 Auto-calibration System Developed to Assimilate AMSR-E Data into a Land Surface

1100 Model for Estimating Soil Moisture and the Surface Energy Budget. *Journal of the*

1101 *Meteorological Society of Japan*, *85A*, 229–242. https://doi.org/10.2151/jmsj.85A.229,

1102 2007.

1103

1104 Zhang, D., Madsen, H., Ridler, M. E., Refsgaard, J. C., and Jensen, K. H.: Impact of

1105 uncertainty description on assimilating hydraulic head in the MIKE SHE distributed

1106 hydrological   model,   *Advances   in   Water   Resources,   86,*   400-413,

1107 https://doi.org/10.1016/j.advwatres.2015.07.018, 2015.

1108

1109 Zhang, F., Snyder, C., and Sun, J.: Impacts of Initial Estimate and Observation

1110 Availability on Convective-Scale Data Assimilation with an Ensemble Kalman Filter.

1111 *Monthly. Weather. Review.,* **132**, 1238–1253, https://doi.org/10.1175/1520-

1112 0493(2004)132<1238:IOIEAO>2.0.CO;2, 2004

1113

1114 Zhang, H., Kurtz, W., Kollet, S., Vereecken, H., and Franssen, H. J. H.: Comparison of

1115 different assimilation methodologies of groundwater levels to improve predictions of root

1116 zone soil moisture with an integrated terrestrial system model. *Advances in Water*

1117 *Resources*, *111*, 224–238. https://doi.org/10.1016/j.advwatres.2017.11.003, 2018.

1118

1119

1120

1121

122

123 **Table 1.** Configuration of the data assimilation experiments in section 3.1.

	hydraulic conductivity [m/h]	observation's location [m]
LOW_K-UP_O	0.005	2500
LOW_K-DOWN_O	0.005	1500
HIGH_K-UP_O	0.02	2500
HIGH_K-DOWN_O	0.02	1500

124

125 **Table 2.** Configuration of the data assimilation experiments in section 3.2

	overland flows	observing network
noOF_NoDA	none	no data assimilation
noOF_DA_obs1	none	Figure 7a
noOF_DA_obs9	none	Figure 7b
noOF_DA_obs361	none	Figure 7c
OF_NoDA	simulated	no data assimilation
OF_DA_obs1	simulated	Figure 7a
OF_DA_obs9	simulated	Figure 7b
OF_DA_obs361	simulated	Figure 7c

126

127

128

129

130

131
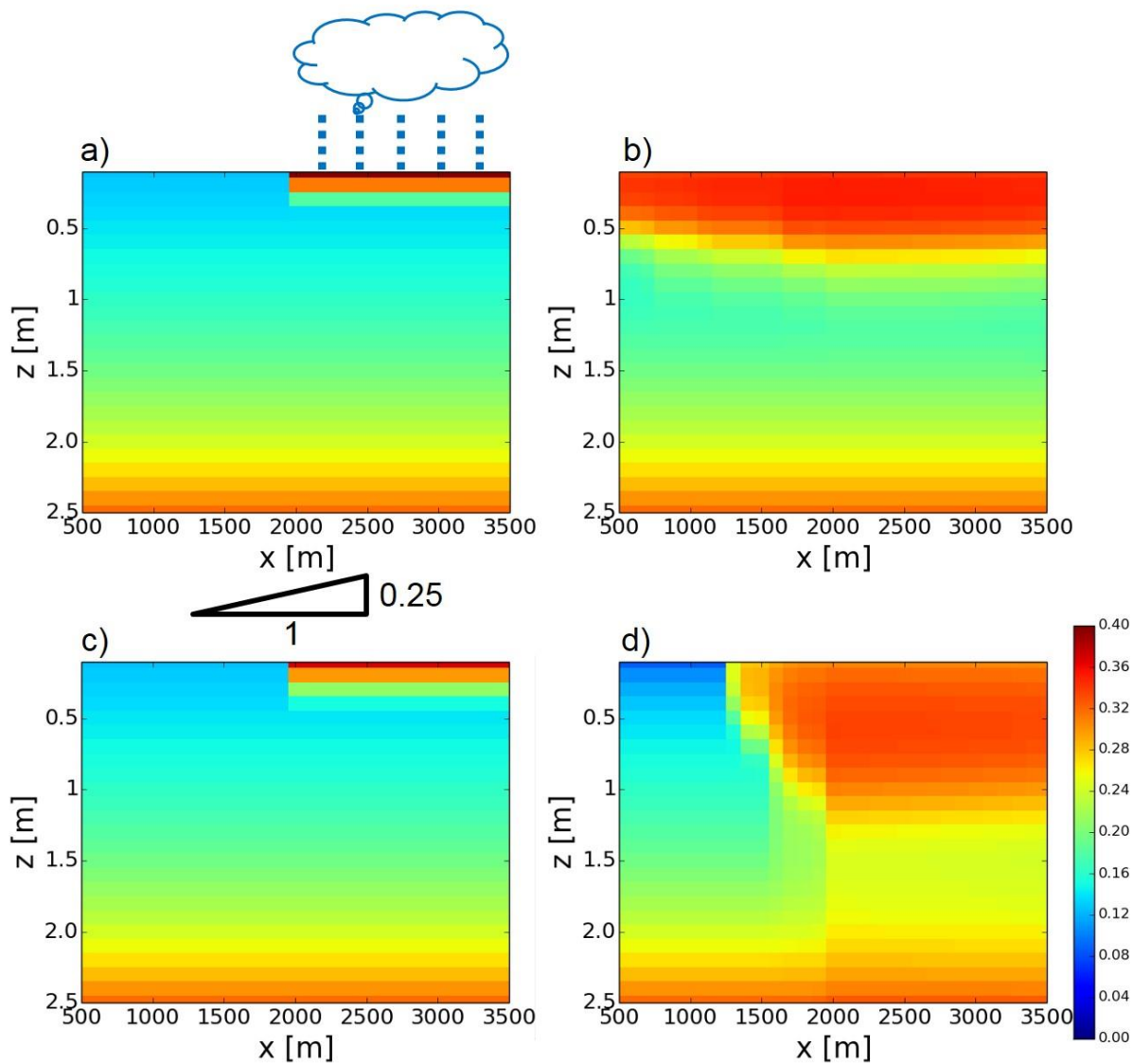
Figure 1. Distributions of volumetric soil moisture simulated by the synthetic reference runs. (a) The

distribution of volumetric soil moisture [m^3/m^3] simulated by the LOW_K synthetic reference run at t = 0h.

The schematic of the configuration of the synthetic reference runs is also shown (see also section 3). (b) same

as (a) but at t = 130h. (c,d) same as (a,b) but for the HIGH_K synthetic reference run.

136

137
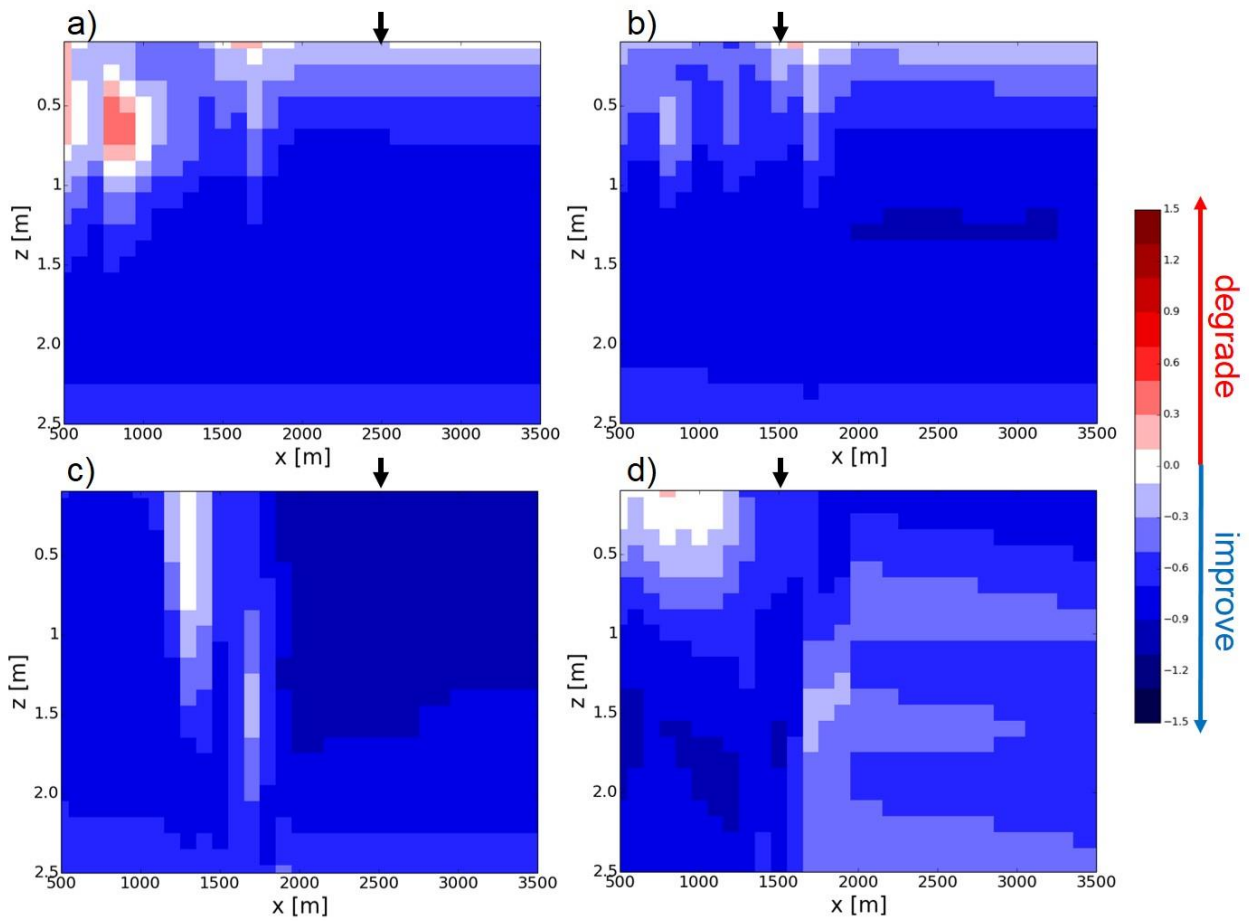
Figure 2. The improvement rates of the (a) LOW_K-UP_O, (b) LOW_K-DOWN_O, (c) HIGH_K_UP_O,

(d) HIGH_K-DOWN_O experiments (see Table 1 and section 3). Black arrows show the locations of the soil

moisture observations in each experiment.

141

142
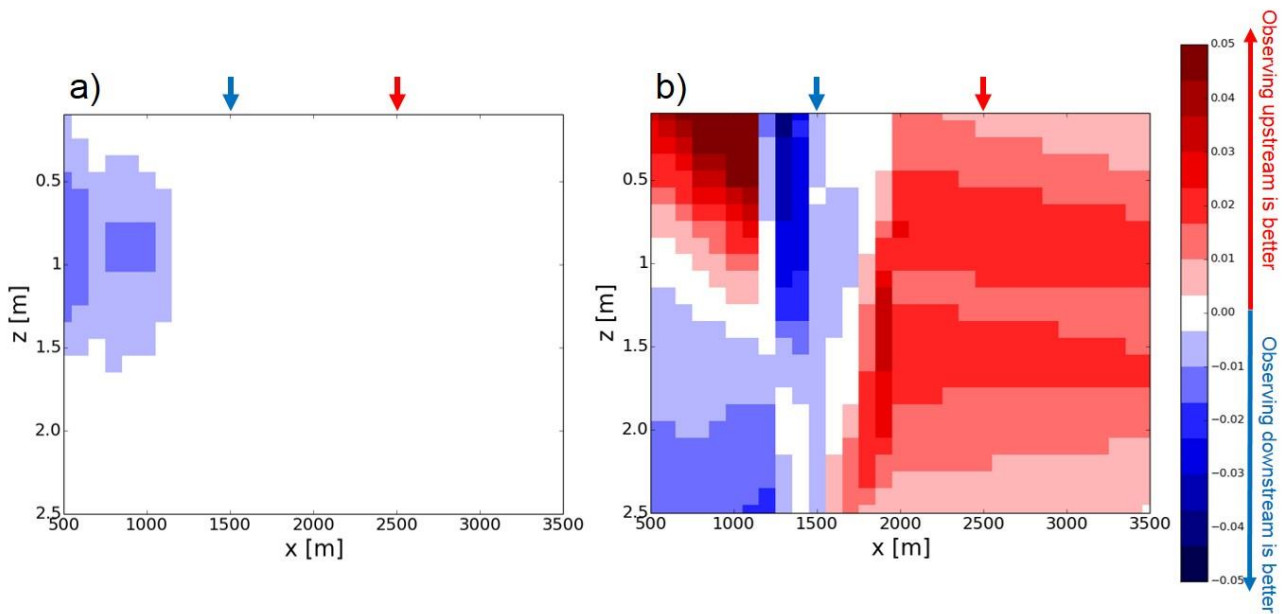
Figure 3. (a) The difference of time-mean RMSEs between the LOW_K-UP_O and LOW_K-DOWN_O

experiments (see Table 1 and section 3). Red (blue) color indicates that the observations in the upper (lower)

part of the slope reduce time-mean RMSE by data assimilation better than those in the lower (upper) part of

the slope (see also arrows which are the locations of the observations). (b) same as (a) but for the difference

between the HIGH_K-UP_O and HIGH_K-DOWN_O experiments.

148

149
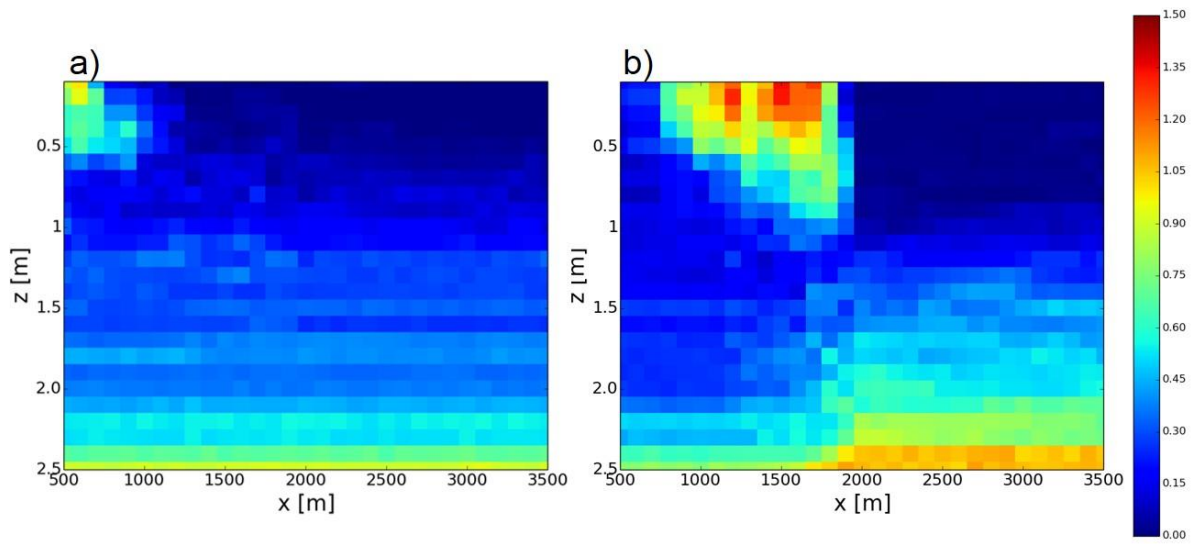
Figure 4. The Kullback-Leibler divergence of the NoDA experiment generated by (a) the LOW_K reference

and (b) the HIGH_K reference at t = 130h (see also Figure 1b and 1d).

152

153
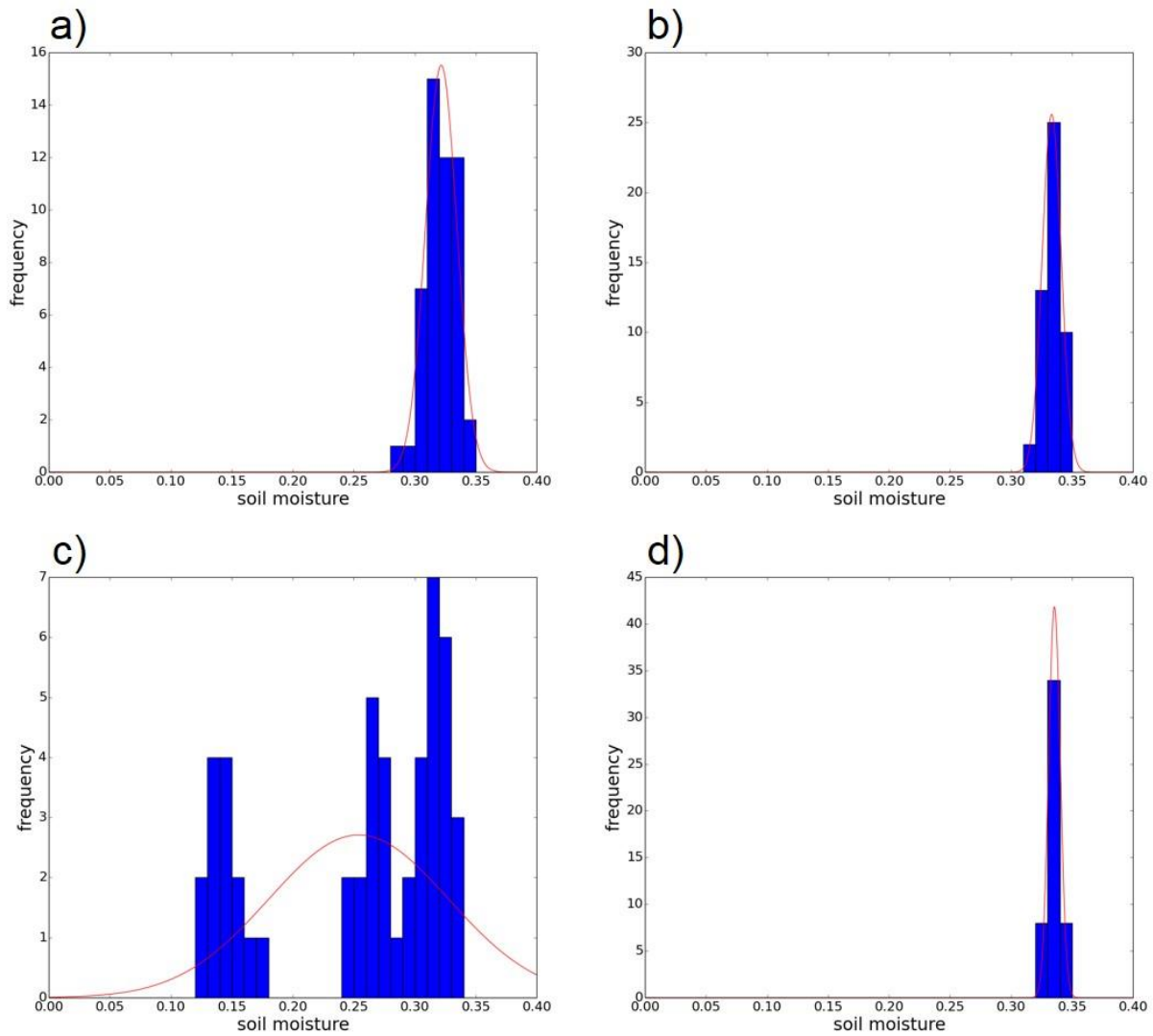
Figure 5. (a) The histogram (blue bars) of the volumetric soil moisture simulated by the NoDA experiment

(see section 3) with the LOW_K reference at x=1500m, z=0.5m, and t=130h (see also Figure 4). Red line

shows the Gaussian distribution with the mean and variance sampled by the ensemble. (b) same as (a) but at

x=2500m, z=0.5m, and t=130h. (c) same as (a) but for the HIGH_K reference. (d) same as (c) but at x=2500m,

z=0.5m, and t=130h.

159

160

161
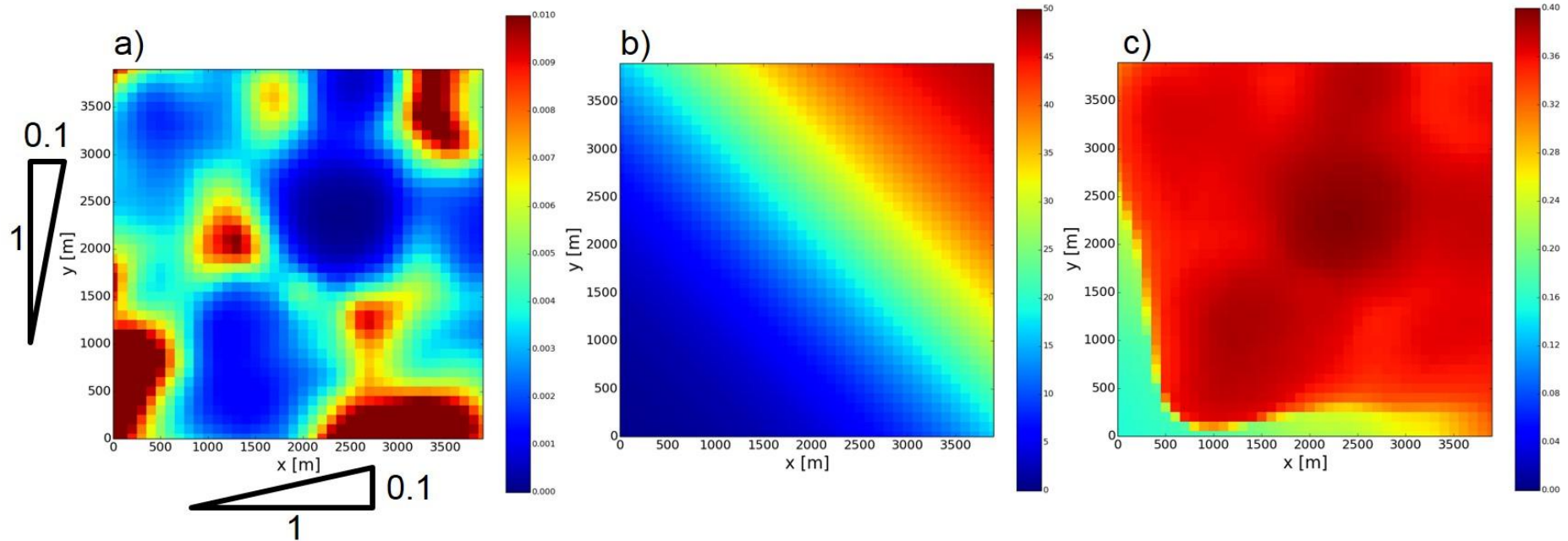
Figure 6. (a) Distribution of surface saturated hydraulic conductivity [m/h] in the synthetic reference. (b) Distribution of rainfall rate [mm/h] in the synthetic

reference. (c) Surface volumetric soil moisture [m^3/m^3] at t = 5 [h] in the synthetic reference.

164
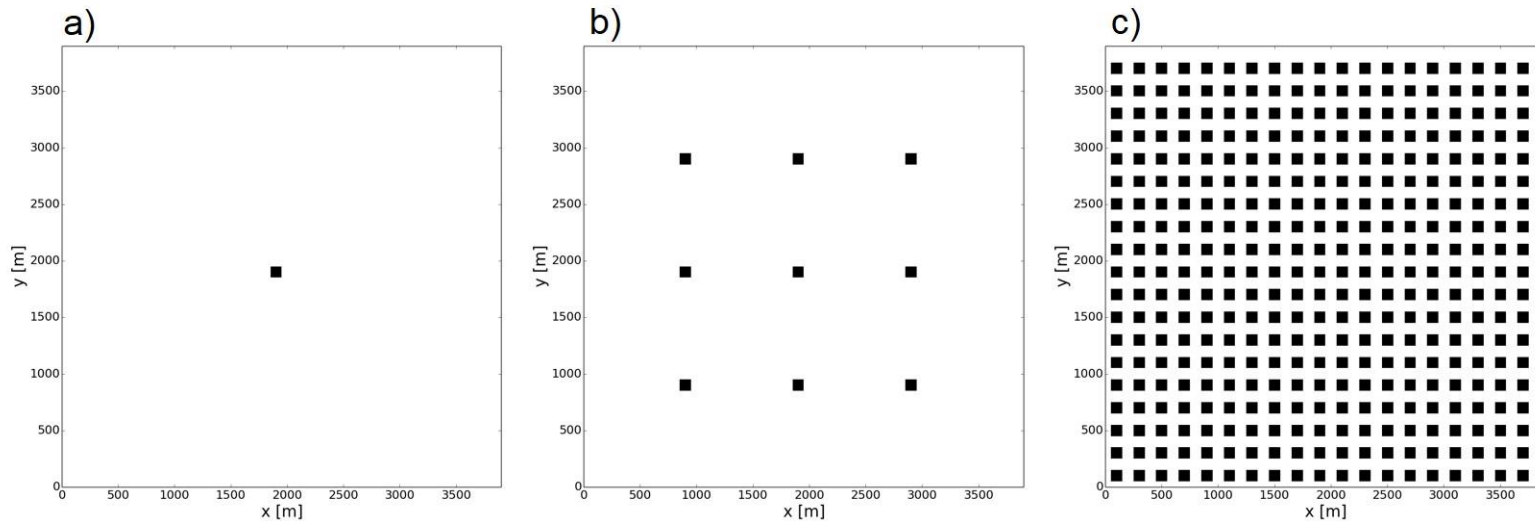
165

166   **Figure 7.** Observing networks. Black boxes are observed grids. (a) obs1, (b) obs9, (c) obs361 See also section 3.2.1.

167

168
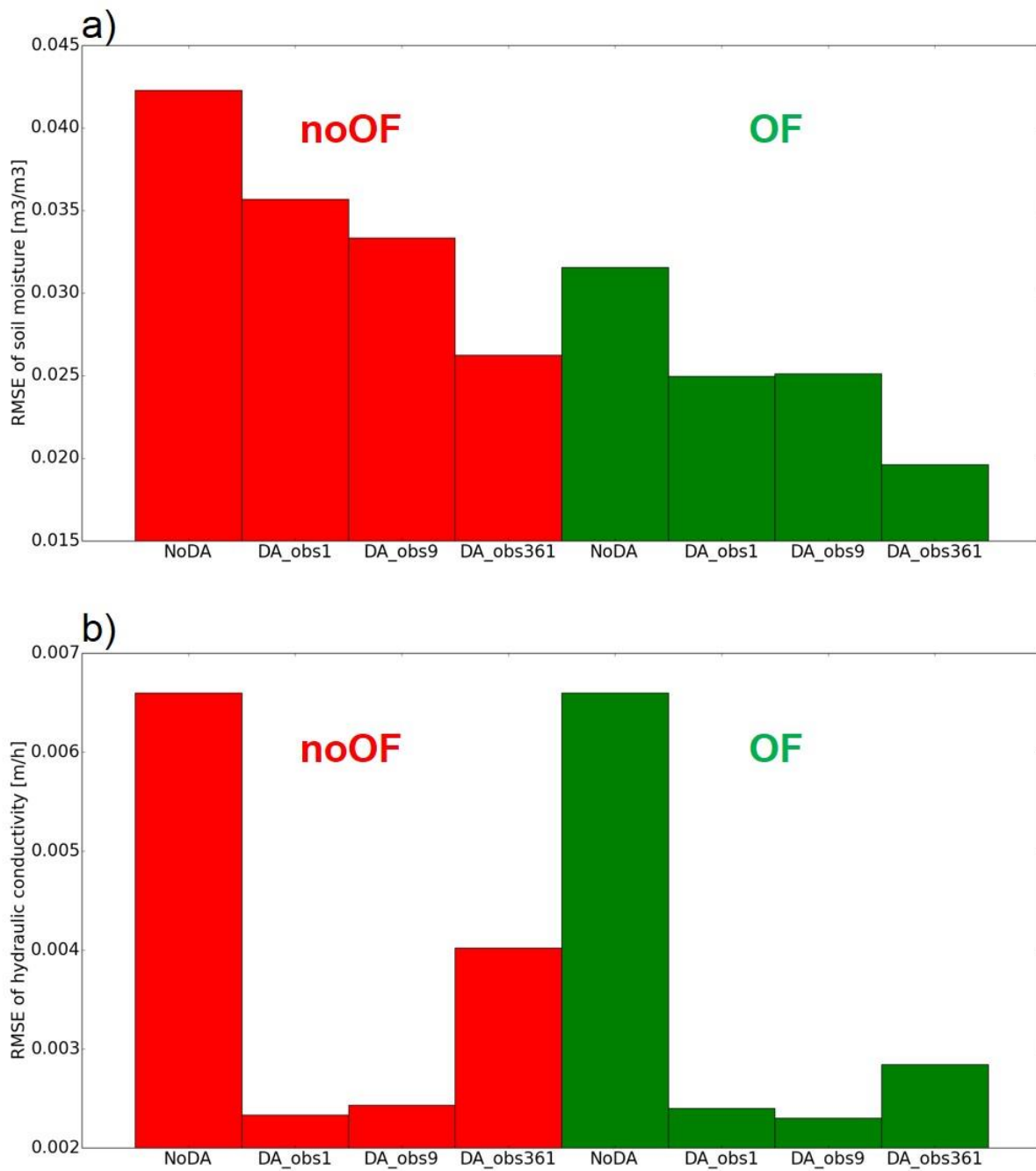
Figure 8. Time-mean RMSEs of the estimation of (a) soil moisture and (b) hydraulic conductivity. Red and

green bars are results of the noOF and OF configuration, respectively (see section 3.2.1 and Table 2).

169

170

171

172

173
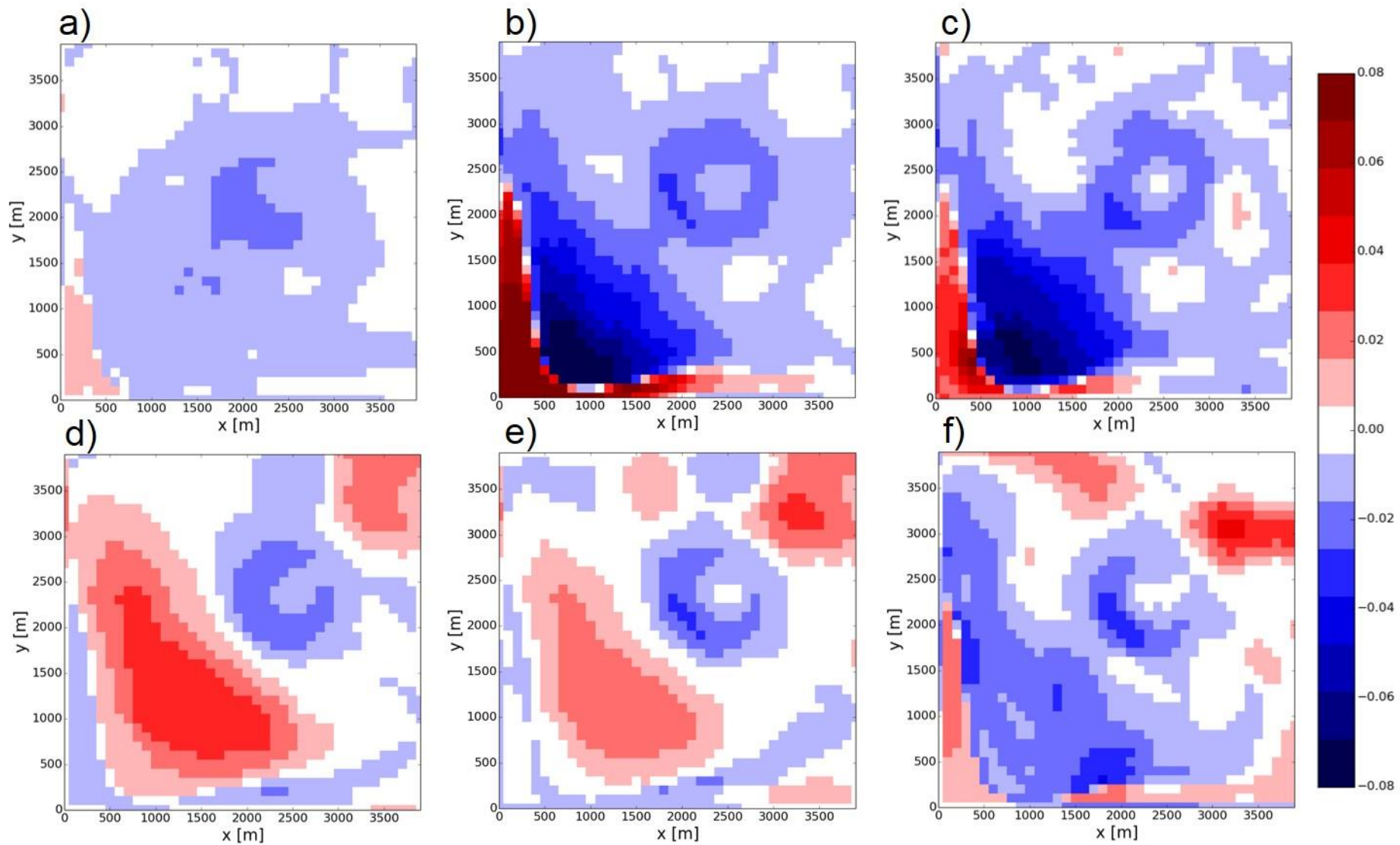
Figure 9. Differences of time-mean soil moisture RMSEs between the DA experiments and the OF_NoDA experiment. (a) OF_DA_obs1, (b) OF_DA_obs9 (c)
OF_DA_obs361 (d) noOF_DA_obs1, (e) noOF_DA_obs9, (f) noOF_DA_obs361.

176
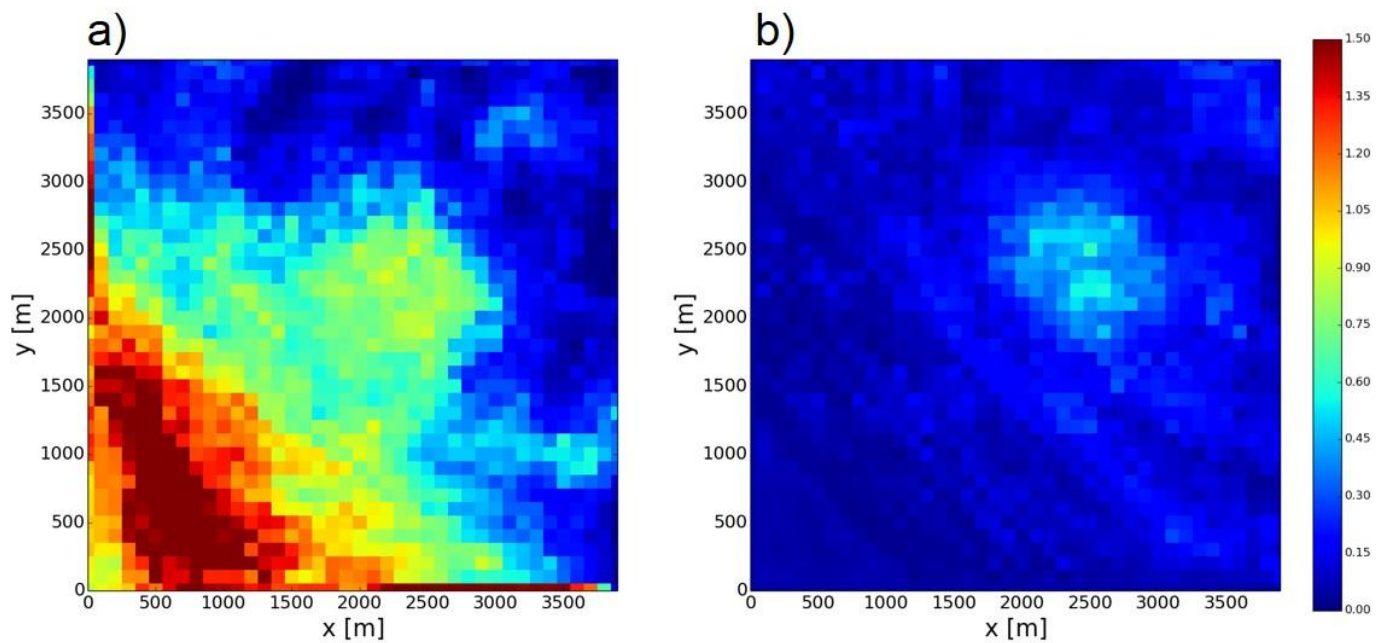
177
Figure 10. The Kullback-Leibler divergence of ensemble members generated by the (a) OF_NoDA and (b)
noOF_NoDA experiments at t = 4 [h].

180
181